

# Bayesian Estimation of Surface Strain Rates from GNSS Measurements: application to the Southwestern US

C. Pagani<sup>1</sup>, T. Bodin<sup>1</sup>, M. Métois<sup>1</sup>, C. Lasserre<sup>1</sup>

<sup>1</sup>Univ Lyon 1, ENSL, CNRS, LGL-TPE, F-69622, Villeurbanne, France

## Key Points:

- A Bayesian interpolation scheme is applied to derive strain rates from discrete geodetic horizontal velocities
- Full probability density functions are provided for spatial derivatives of the 2D velocity field.
- Consistent estimates of strain rates are obtained without underlying physical model nor ad-hoc smoothing parameter.

---

Corresponding author: Marianne Metois, [Marianne.metois@univ-lyon1.fr](mailto:Marianne.metois@univ-lyon1.fr)

## Abstract

Seismic hazard assessment in active fault zones can benefit of strain rate measurements derived from geodetic data. Producing a continuous strain rate map from discrete data is an inverse problem traditionally tackled with standard interpolation schemes. Most algorithms require user-defined regression parameters that determine the smoothness of the recovered velocity field, and the amplitude of its spatial derivatives. This may lead to biases in the strain rates estimation which could eventually impact studies on earthquake hazard. Here we propose a transdimensional Bayesian method to estimate surface strain rates from GNSS velocities. We parameterize the velocity field with a variable number of Delaunay triangles, and use a reversible jump Monte-Carlo Markov Chain algorithm to sample the probability distribution of surface velocities and spatial derivatives. The solution is a complete probability distribution function for each component of the strain rate field. We conduct synthetic tests and compare our approach to a standard b-spline interpolation scheme. Our method is more resilient to data errors and uneven data distribution, while providing uncertainties associated with recovered velocities and strain rates. We apply our method to the Southwestern US, an extensively studied and monitored area and infer probabilistic strain rates along the main fault systems, including the San Andreas one, from the inversion of interseismic GNSS velocities. Our approach provide a full description of the strain rate tensor for zones where strain rates are highly contrasted, with no need to manually tune user-defined parameters. We recover sharp velocity gradients, without systematic artifacts.

## 1 Introduction

### 1.1 Surface strain, fault behavior and space geodesy

Imaging and quantifying the present-day lithospheric deformation is crucial to understanding how and where long-term tectonic loading is accommodated. Plate tectonics theory assumes that the relative motion of rigid lithospheric blocks is accommodated on a limited set of localized fault zones, where the lithosphere either deforms elastically during the interseismic period of the seismic cycle, or in a brittle way during the coseismic rupture (Le Pichon, 1968; Morgan, 1968; Isacks et al., 1968). In a simple elastic framework, the surface deformation generated by slip on a dislocation buried in an elastic half-space can be computed (e.g. Okada, 1985), as well as the surface deformation produced



by full or partial locking of the buried fault using the “backslip” hypothesis (Savage, 1983). Analysing the spatial patterns of surface deformation and their temporal variations around active faults can therefore help constraining the behaviour of fault systems at each stage of the seismic cycle.

With the advent of space geodesy in the 1990s, and in particular the growing development of GNSS (Global Navigation Satellite System) networks in active fault zones, precise measurements of surface displacements made it possible to detect and model various processes of tectonic deformation, thus revolutionizing our understanding of fault seismic cycle (e.g. Bürgmann & Thatcher, 2013). The last decades have seen the number of geodetic observations of large earthquakes and interseismic strain along major faults increase significantly (e.g. Blewitt et al., 2018). Combined with an improved knowledge of the past seismic history of faults, such observations have highlighted a spatial correlation between portions of the seismogenic zone locked during the interseismic period and the coseismic rupture zones, while portions of faults aseismically slipping during the interseismic phase appeared as potential nucleation zones or barriers to earthquakes (e.g. Chlieh et al., 2008; Simons et al., 2011; Métois et al., 2016). This paved the way to provide plausible scenarios for future earthquakes based on the monitoring of interseismic surface strain (e.g. Kaneko et al., 2010; Avouac, 2015; Beauval et al., 2018).

If most of the deformation due to relative block motions is indeed taken up on well localized and mapped plate boundaries, the lithosphere can also deform in a more diffuse way on wider zones, in particular in and around collisional belts (e.g. Thatcher, 2009). Such diffuse deformation may be accommodated elastically by series of multiple active faults, or through other non-elastic processes within the lithosphere (England & Molnar, 1997; Copley, 2008; D’Agostino et al., 2014). In combination with geological, tectonic and seismological data, geodetic measurements of surface deformation can then help to refine the degree of localization of the deformation over wide intracontinental areas, to identify active structures and constrain the style of the deformation, as well as the underlying mechanical processes.

Modern geodetic techniques now offer measurements of surface velocities with accuracy of the order of 1mm/yr or below for the interseismic period. They each have their own contributions and specificities concerning the components of the ground motion that they capture, their resolution and their uncertainties, and appear to be very complemen-

76 tary. While horizontal and vertical motion can be measured by GNSS and optical im-  
 77 age correlation, Interferometric Synthetic Aperture Radar (InSAR) only provide the pro-  
 78 jection of ground displacements in the line-of-sight (LOS) of the satellite. GNSS mea-  
 79 surements remain spatially sparse, at discrete stations, but benefit from a temporal sam-  
 80 pling up to  $\simeq 1\text{Hz}$ . Space geodesy based on optical and radar images, on the contrary,  
 81 provide data at all satellite image pixels, with a temporal resolution dependent on the  
 82 return time of the satellites. Finally, depending on the technique, uncertainties can be  
 83 spatially and temporally correlated or not. Taking advantage of the large amount and  
 84 diversity of geodetic data available today to constrain spatio-temporal variations of the  
 85 strain rate field is a challenge for the community involved in seismic hazard studies.

## 86 1.2 The strain rate tensor : formulation, assumptions and analysis

87 The variations of the strain rate field can be explored through the analysis of the  
 88 velocity gradient  $\nabla V = \partial_i V_j$ , its symmetrical part, and the *strain rate tensor*  $\dot{\epsilon}_{ij} =$   
 89  $\frac{1}{2}(\partial_i V_j + \partial_j V_i)$ . Spotting regions with high strain rates may help identify active faults  
 90 prone to high seismic hazard (e.g. Elliott et al., 2016). To this end, maps of the second  
 91 invariant  $I_2$  of  $\dot{\epsilon}$  are built either at the local to regional scale (e.g. D’Agostino, 2014; Metois  
 92 et al., 2015), or at the continental to global scale (e.g. Kreemer et al., 2014). Following  
 93 P  rouse et al. (2012); D’Agostino (2014) and Metois et al. (2015), we define the second  
 94 invariant of the horizontal strain rate tensor as :

$$95 \quad I_2 = \sqrt{\dot{\epsilon}_{xx}^2 + \dot{\epsilon}_{yy}^2 + 2\dot{\epsilon}_{xy}^2}.$$

96 Note that most GNSS studies only consider the horizontal 2D tensor  $\dot{\epsilon}$  (Ward, 1998;  
 97 D’Agostino, 2014) or a partially 3D tensor (Mazzotti et al., 2011; Shen et al., 2015) for  
 98 two main reasons : (1) the vertical component of the GNSS velocity is often associated  
 99 with large uncertainties (Bennett & Hreinsd  ttir, 2007), and (2) we have no access to  
 100 the vertical derivative of the velocity components ( $\partial_z V_x, \partial_z V_y, \partial_z V_z$ ). Joint GNSS-InSAR  
 101 studies also remain limited to a 2D strain tensor analysis (e.g. Weiss et al., 2020). In this  
 102 study, we only consider the horizontal velocity field and corresponding 2D strain rate ten-  
 103 sor, while discussing in section 6 the possibility to include  $V_z$  in future analysis .

104 Providing continuous maps of the different components or combinations of com-  
 105 ponents of the horizontal strain tensor can help to understand the tectonic regime and

style of deformation of a given area (e.g. Pérouse et al., 2012; Metois et al., 2015; Chousianitis et al., 2015; Kreemer et al., 2018). For example, the second invariant analysis gives clues on the variations of strain amount and localization across faults. The divergence of the velocity field  $d = tr(\dot{\epsilon})$  highlights areas experiencing dilation or compression (a positive divergence stands for dilation while negative divergence is compression), while the horizontal vorticity defined as  $rotV = \partial_x V_y - \partial_y V_x$  allows the identification of nearly rigid blocks. The principal directions of the strain rate tensor may also be compared to directions of stress when the lithosphere is considered fully elastic. They are therefore often plotted against focal mechanisms or long-term stress orientations related to the geological setting (e.g. England et al., 2016; Mathey et al., 2020).

In the past decades, the geodetically-derived strain rate tensor has also been used to derive the equivalent seismic energy stored as elastic deformation that could be released during earthquakes. In particular, Ward (1998) proposes to use the formula from Kostrov (1974) to calculate geodetic moment rates  $\dot{M}_o^g$  from  $\dot{\epsilon}$ , in the case of a uniaxial strain. For a region of given area  $A$ , its geodetic moment rate is expressed as :

$$\dot{M}_o^g = 2\mu H_s A \dot{\epsilon}_{max}, \quad (1)$$

where  $\mu$  is the rigidity modulus,  $H_s$  the seismogenic thickness, and  $\dot{\epsilon}_{max}$  is the largest eigenvalue of the strain rate tensor  $\dot{\epsilon}$ . Comparing  $\dot{M}_o^g$  to the released seismic energy based on historical and instrumental seismic catalogues provides information on the energy that remains to be released either seismically or aseismically (Ward, 1998; Pancha et al., 2006; Mazzotti et al., 2011; Angelica et al., 2013; D’Agostino, 2014).

### 1.3 Aim of the study

As shown above, mapping continuous surface velocities together with their spatial derivatives and associated uncertainties can benefit a broad community. However, two main methodological limitations remain:

1. As in-situ geodetic data provide spatially discrete and unevenly distributed information on the surface displacement rate, these data need to be interpolated in order to recover a continuous strain rate map. This also applies to InSAR data in case of low coherence. Such computing formally constitutes an inverse problem with a highly non-unique solution and a strong trade-off between model complex-

ity and model constraints, i.e. between the level of spatial resolution and the level of errors in the solution (Bodin, Sambridge, et al., 2012).

2. Uncertainties on the interpolated velocity field and their propagation onto the strain rate tensor components are often poorly estimated. These uncertainties are nonetheless required and crucial if we want geodetic estimates of the strain rates to integrate probabilistic seismic hazard assessment schemes (Beauval et al., 2018; Gerstenberger et al., 2020).

In this paper, we propose to tackle these issues by applying a transdimensional Bayesian approach (Bodin, Salmon, et al., 2012) to the strain rate reconstruction problem. We first describe the different approaches used in the community to produce strain rate maps. We then present our inversion method and illustrate its potential benefits with synthetic tests. Because the San Andreas fault system has been extensively studied in the past and is particularly well instrumented, we build our synthetic tests from its simplified geometry and kinematics. We then propose a first application to real observations of a GNSS velocity field spanning the interseismic deformation across this fault system and the South-western US. Finally, we discuss the main outcomes, advantages and limitations of the proposed method. We show that we are able to provide a full probabilistic description of the strain rate tensor for zones where strain rates are highly contrasted, with no need to introduce user-defined parameters. Our method recovers sharp velocity gradients, therefore localizing strain, and distinguishing creeping from locked fault segments, without systematic biases.

## 2 Inverting for the strain rate tensor : state of the art

Since the first geodetic observations of ground movements by triangulation or levelling (e.g. Frank, 1966; Savage & Burford, 1970), several methods have been developed to infer surface strain rates from velocity fields. Today, they mainly use GNSS data (e.g. Shen et al., 1996; Vergnolle et al., 2007; Kreemer et al., 2018; Masson et al., 2019) and start to incorporate space geodetic data from InSAR and optical imagery (e.g. H. Wang et al., 2019; Barnhart et al., 2020a). Some of these methods rely on geophysical models, such as elastic or visco-elastic block models with predefined active faults (e.g. McCaffrey et al., 2013; Parsons, 2006), to calculate surface velocity and strain rates. Others aim at deriving the strain rate tensor from surface observations alone, without any underlying physical model.

Among the “model-free” methods, two main approaches coexist in the literature. The most standard approach requires to first spatially interpolate local displacement rates measured at GNSS stations to build a continuous velocity field. The strain rate tensor is then simply obtained by taking the gradient of the interpolated velocity field. The interpolation (or 2D regression) is often conducted by fitting a spline function to the data (Beavan & Haines, 2001; Kreemer et al., 2003; Metois et al., 2015). The level of smoothing to interpolate the velocity field is usually arbitrarily defined by the user. For instance, in the *SPARSE* code developed in Beavan & Haines (2001), it is controlled by the interpolation grid spacing and the variance attributed to each grid cell (it can therefore be spatially variable). In the adjusted bi-cubic spline-in-tension method (referred to as the B-spline method in the following), a tension parameter must be chosen as well (Smith & Wessel, 1990; Wessel & Bercovici, 1998; Gan et al., 2007; Wessel & Becker, 2008; Hackl et al., 2009). This tension parameter is unique for the whole study area. In the case of unevenly spaced geodetic data, regions with the densest sampling may thus be over-smoothed and information may be lost. Other interpolation techniques have been proposed to limit this weakness. For instance, the velocity for each cell of the interpolation grid can be computed as the weighted average of velocities at neighboring GPS stations (Mazzotti et al., 2011). However, here again, the weighting function defining the smoothness of the solution needs to be defined by the user. The level of smoothness of the velocity field (i.e. the amplitude of its derivatives) directly determines the amplitude of the strain rate tensor. An arbitrarily fixed smoothing level is therefore a serious limitation to proper strain rate assessment. Finally, B-spline methods are based on a regularized optimization scheme, and thus do not offer any constraint on the uncertainties regarding the velocity field and the strain rate tensor (Aster et al., 2018), which is problematic in the context of hazard assessment.

In a second type of approach, geodetic strain rates are directly inverted from the GNSS data without the need for a velocity interpolation scheme (Shen et al., 1996; Spakman & Nyst, 2002; Ward, 1998). At each point on a regular geographical grid, assuming a constant strain rate field, a system of linear equations can relate the displacement and deformation at that point and GPS velocities at neighbouring stations. The observed velocities at GPS stations can thus be inverted through a standard least-square scheme to recover the unknown deformation at any given point. This method offers more robust strain rate estimates as such rates are directly computed as weighted averages. It pro-

vides also a first-order estimate on strain uncertainties. Many studies have used such least-square inversion schemes for studying surface deformation in specific areas, as for instance Sagiya et al. (2000) in Japan, Chousianitis et al. (2015) in Greece, or Palano et al. (2018) in Iran. However, the parameter controlling the weighting decay with distance in the least-square inversion remains again arbitrarily-chosen, and acts as a smoothing factor that affects the resulting solution. Efforts have been made to optimize the level of smoothing and to account for spatial variability of data density (Shen et al., 2007, 2015). In particular, Kreemer et al. (2018) propose an algorithm in which, for any given evaluation point, multiple least-square inversions from different stations triplets are conducted. The median strain rates over the ensemble of inverted ones are then provided at that point.

However, the standard techniques presented above remain sensitive to the GNSS network geometry (with unevenly spaced data in most cases), data outliers and ad-hoc user parameters. This is now acknowledged as a major issue in the community, potentially leading to systematic artifacts that could be mis-interpreted as tectonic signals (e.g. Baxter et al., 2011). In the Southwestern US for instance, where seismic hazard is high, a wide range of methods have been applied in the last decades to recover the strain rate tensor (e.g. Hackl et al., 2009; Kreemer et al., 2018), with results that may differ significantly (Sandwell et al., 2010). The remaining limitations in these methods are therefore preventing further integration of geodetic measurements in seismic assessment methods.

In an attempt to overcome such limitations, we propose a method based on Bayesian inference to invert discrete GNSS velocities for the continuous 2D surface displacement field and the associated velocity gradients and strain rate tensor. We follow from the work of Bodin, Salmon, et al. (2012) who proposed a transdimensional Bayesian surface reconstruction algorithm to estimate the Moho topography beneath Australia from a discrete set of local observations. In this approach, the reconstructed surface is parameterized with a mesh that self-adapts to the level of information in the data. This proves to be well suited for very heterogeneous data (spatially or in terms of data type and noise level). Choblet et al. (2014) used the same approach to reconstruct probabilistic maps of relative variations of coastal sea level from tide gauge records. The approach was also used by Husson et al. (2018) to reconstruct maps of vertical displacement rates from GPS measurements, and by Hawkins, Bodin, et al. (2019) and Hawkins, Husson, et al. (2019) to reconstruct maps of sea level rise by combining vertical GPS velocities, satellite al-

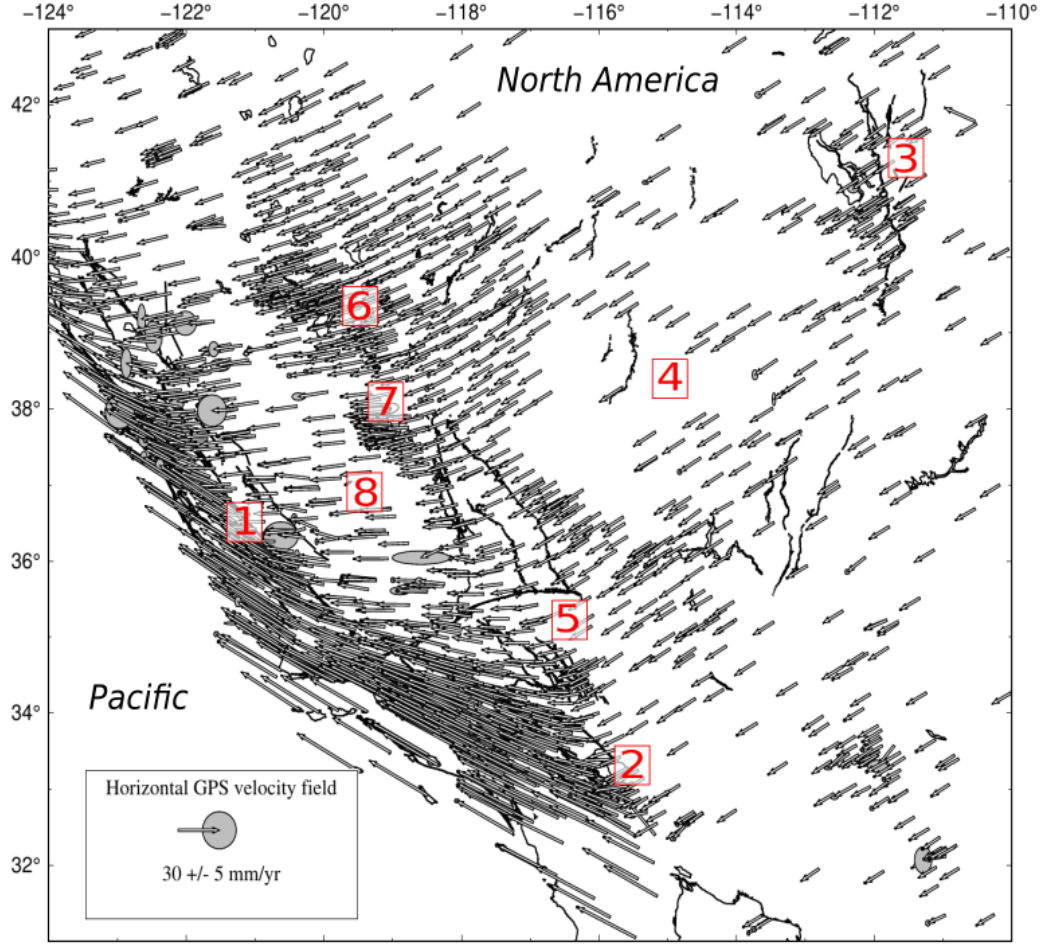


**Figure 1.** Horizontal GPS velocities from the MIDAS dataset in IGS14 reference frame in the Southwestern US (this study area). Ellipses represent the uncertainties at 95% level. Black lines : active faults (Quaternary fault and fold database, 2019). Note that the density of GNSS stations is highly variable and higher near the San Andreas fault system. Key features of this plate boundary zone are labeled : 1- Monarch Peak creeping section (Central section) of the main San Andreas fault, 2- Salton Sea Lake zone, 3- Wasatch mountains fault zone, 4- Basin and Range province, 5- East California Shear Zone, 6- Walker Lane, 7- Long Valley Caldera, 8- Central Valley and Sierra Nevada.

timetry and tide gauge measurements. In this work, the reconstructed surface is defined by two parameters : the two components of the interseismic horizontal velocities measured at GNSS stations. Details of the method are presented in section 4.

### 3 Tectonic context of the Southwestern US and GNSS velocity field

To test and illustrate the potential of our methodology, we need a data set that is heterogeneous in several aspects : heterogeneous in data coverage, with a combination of densely monitored and poorly sampled areas, heterogeneous in data quality with variable uncertainties, and spatially heterogeneous in the expected strain rate amplitude and style.

In all these regards, our study area, located in the Southwestern US ( $31^{\circ}$  to  $43^{\circ}$ N,  $110^{\circ}$  to  $124^{\circ}$ W, see figure 1) is a good test case. The plate boundary between the Pacific and North American plates accommodates  $\simeq 5$  cm/yr of relative right-lateral motion (Altamimi et al., 2017) partitioned over several active structures. The most famous one is the San Andreas strike-slip fault system that takes up to 78% of the relative plate motion (Freymueller et al., 1999; Bennett et al., 2003), the remaining motion being accommodated on a set of distributed active faults further inland. Eastward, the Sierra Nevada and Central Valley behave as a nearly rigid microplate that moves 11.4 mm/yr Northwestward relative to the stable North American plate (Bennett et al., 2003; Pérouse & Wernicke, 2017). This microplate is bounded to the East by the Walker Lane and East California Shear Zone where right-lateral shearing is dominant, with a small amount of extension, and that hosted significant historical earthquakes (Bennett et al., 2003; Niemi et al., 2004; Wesnousky et al., 2012). The Garlock fault zone, in the vicinity of which occurred the recent Ridgecrest sequence (July 2019, Mw max 7.1 (e.g. K. Wang & Bürgmann, 2020)), is a SW-NE left-lateral strike slip structure perpendicular to the San Andreas and East California Shear Zone (Peltzer et al., 2001a). The large Basin and Range province farther east extends up to the Wasatch mountain belt and is characterized by a series of normal faults accomodating on the order of 3 mm/yr of the relative plate motion (e.g. Niemi et al., 2004). The Wasatch fault zone, marking the boundary between the Basin and Range and the Colorado stable plateau, is the easternmost active structure of the plate boundary zone and is extending at low rates (1-2 mm/yr) that may allow for Mw 7 earthquakes with large recurrence time (Machette et al., 1991; Niemi et al., 2004; Pérouse & Wernicke, 2017).



This complex plate boundary area is one of the best studied fault zones on Earth and geodetic measurements have been conducted there since 1923 (date of the first levelling studies in the Parkfield area) and more extensively since the 1980's (e.g. Snay et al., 1983; Murray & Langbein, 2006). Since then, modern GNSS networks have been installed to monitor the ongoing surface deformation, for instance in the framework of the PBO (Herring et al., 2016), NEARNET/MAGNET (B. Hammond et al., 2010), or SCIGN (Hudnut et al., 2001) initiatives. The observed deformation is due to a wide variety of physical phenomena : eulerian plate or microplate motions (Altamimi et al., 2016), interseismic loading on active faults (e.g. Peltzer et al., 2001b; McCaffrey, 2005), coseismic and postseismic deformation due to relatively moderate but destructive earthquakes (e.g. Shen et al., 1994; Murray & Langbein, 2006; Milliner & Donnellan, 2020), volcanic inflation and deflation of the Long Valley caldera (e.g. Marshall et al., 1997; W. Hammond et al., 2019), and hydrological depletion or infill of aquifers in particular in the Central Valley (Amos et al., 2014; Chaussard et al., 2017) or elsewhere (Silverii et al., 2020).

To represent the current deformation in Southwestern US, we choose here to use the MIDAS (Median Interannual Difference Adjusted for Skewness) velocity field that compiles long-term velocities derived from GNSS daily times-series. It is provided by the Nevada Geodetic Laboratory (Blewitt et al., 2016, 2018). In our study area, the MIDAS data set (downloaded on February 2020) provides velocities for 2441 stations of various local networks (PBO, MAGNET, SCIGN) gathered in the Network of the Americas (NOTA, see figure 1). The velocities are calculated on the 1994 to 2020 time-span in the IGS14 reference frame. In the densest parts of the velocity field, in particular near the San Andreas fault or in the Long Valley Caldera, baselines are around 10 km (even shorter near some large city centers), while they reach more than 250 km in the less densely instrumented areas within the Basin and Range (figure 1).

The MIDAS algorithm computes velocities for each individual time-series as the median of the linear trends obtained between two dates separated by approximately one year (Blewitt et al., 2016). As a result, MIDAS estimated velocities should be less affected by seasonality than when using classical regressions, and give robust estimates for surface average velocities (W. C. Hammond et al., 2016), except where non-linear deformation occurs such as post-seismic deformation or multi-annual hydrological loading. This is not the case in our study area for the considered time-span, therefore we assume that the data set mostly captures the interseismic deformation in the area. We remove

only 4 stations from our data set, either because their velocities were computed on a too short time-span (lower than one year) or because their velocities were larger than 150  $mm/yr$  on at least one component. In our study area, average uncertainties are of 0.31, 0.28 and 0.81  $mm/yr$  on the East, North and Up components, respectively. The uncertainties estimated by the MIDAS algorithm may be considered slightly overestimated compared to those obtained with usual techniques for long and clean time series (Mazzotti et al., 2020). However, because we chose to use on purpose the raw MIDAS interseismic velocity field provided online, without very restrictive quality criterion (see above), our data set may still include velocities that are not fully consistent with the long-term interseismic trends (when calculated on a too short time period or in cases of large data gaps for instance). To take into account this remaining heterogeneity in the data set, we thus chose to increase the MIDAS uncertainties by 10%. In the Bayesian inversion carried out in this study, we assume that errors affecting the velocities are Gaussian, uncorrelated between different stations and independent on each horizontal component. This is a strong first-order hypothesis. Indeed, the structure of noise on a single GPS station is usually considered to be composite, both white and flicker (Williams et al., 2004; Santamaría-Gómez et al., 2011), and spatially correlated noise has been identified on regional to global scale (also called common-mode error, see (Wdowinski et al., 1997; Dong et al., 2006; Benoist et al., 2020)). This hypothesis and its implications will be discussed further in section 6.

Other velocity estimates have been published for this region (e.g. McCaffrey, 2005; Klein et al., 2019) and may be substantially different from the MIDAS data set (either because they cover a different time-span or because of different post-processing choices). However, our paper aims at demonstrating the potential of our inversion method whatever the chosen inverted data set.

To assess the behavior and the performances of our algorithm, we first create a realistic synthetic set of velocity measurements that mimics the real MIDAS velocity field described above. We compute a theoretical (target) velocity field, and sample it at each GNSS station used in MIDAS (see section 5.1 for details on the synthetic model used). We then add random Gaussian errors to each measurement with a variance as given by MIDAS uncertainties. In a second step, we apply the inversion scheme to the real MIDAS velocity field described above. Both data sets share the exact same characteristics

and can be considered as an ensemble of displacement rates measured at  $n$  GNSS stations that can be formally described by the vector:

$$\mathbf{d}_{\text{obs}} = \begin{bmatrix} (V_{x_1}, V_{y_1}), \\ \dots, \\ (V_{x_n}, V_{y_n}) \end{bmatrix}$$

where  $(V_{x_i}, V_{y_i})$  define the observed ground velocities for the  $i^{\text{th}}$  of our  $n$  GNSS stations used as an input. Similarly, uncertainties associated with these observations are given by a vector

$$\sigma_{\text{obs}} = \begin{bmatrix} (\sigma_{x_1}, \sigma_{y_1}), \\ \dots, \\ (\sigma_{x_n}, \sigma_{y_n}) \end{bmatrix}$$

## 4 Method: Inverting for the geodetic strain rate

### 4.1 Parameterizing the velocity field

To parameterize the continuous horizontal velocity field at the surface, we use a set of nodes scattered on the surface as represented in red in figure 4.1. A horizontal velocity vector is assigned to each node. Note that nodes are independent of the location of the GNSS stations: their number, position, and velocity value are unknown parameters to be inverted for. They can be freely modified during the inversion. This surface parametrization is given by the vector:

$$\mathbf{m} = \begin{bmatrix} k, & (N_{x_1}, N_{y_1}, x_1, y_1), \\ \dots, \\ (N_{x_k}, N_{y_k}, x_k, y_k) \end{bmatrix}$$

where  $k$  is the number of nodes, and  $(N_{x_j}, N_{y_j}, x_j, y_j)$  define the horizontal velocities and position for the  $j^{\text{th}}$  node of the parametrization.

A continuous planar surface can be constructed from the vector  $\mathbf{m}$ . The nodes are used to partition the plane into Delaunay triangles, so that no node is inside the circum-

circle of any triangle. The velocity field within a triangle is then defined by a linear interpolation between the velocities assigned at each node defining the triangle. Within each triangle, the velocity field is a linear function of space, and the gradient (which is constant within the triangle) can be obtained from the node velocities through an analytical expression.

Delaunay triangulation schemes have previously been used to compute geodetic strain rates (Kreemer et al., 2018). In these techniques, the vertices are usually fixed, for example at the location of GNSS stations (Cai et al., 2008; Farolfi & Del Ventisette, 2017). In contrast, we propose here an evolutive triangulation : the nodes' location and velocity are the unknown of the inversion and will adapt to the level of information provided by the data.

Additional nodes are added at the four corners of the area of interest to insure that every point in this area is within the convex hull of the Delaunay triangulation.

## 4.2 Bayesian inference

The solution  $\mathbf{m}$  of our regression problem is clearly non-unique, and a Bayesian approach can be used to represent the solution in probabilistic terms (Tarantola, 2005). In a Bayesian framework, the solution to the inverse problem is the *a posteriori* probability density function (PDF), that is the probability of the model parameters  $\mathbf{m}$  given the observed data  $\mathbf{d}_{\text{obs}}$ . It can be written through Baye's theorem:

$$p(\mathbf{m}|\mathbf{d}_{\text{obs}}) = \frac{p(\mathbf{m})p(\mathbf{d}_{\text{obs}}|\mathbf{m})}{p(\mathbf{d}_{\text{obs}})} \quad (2)$$

where  $p(\mathbf{m})$  is the *a priori* probability distribution on the model (or prior), which represents our knowledge about the model before observing the data. In this work, we assume minimal prior knowledge, and use a uniform prior distribution within a reasonable range for each parameter.  $p(\mathbf{d}_{\text{obs}})$  is the evidence and can be ignored here as it is constant and does not depend on  $\mathbf{m}$ .

The term  $p(\mathbf{d}_{\text{obs}}|\mathbf{m})$  is the likelihood distribution. It represents the probability of observing the data given the model and the distribution of data errors. Assuming that data errors are normally distributed with standard deviations given by  $\sigma_{\text{obs}}$ , the likelihood can be related to a  $L_2$  misfit function, and expressed as:

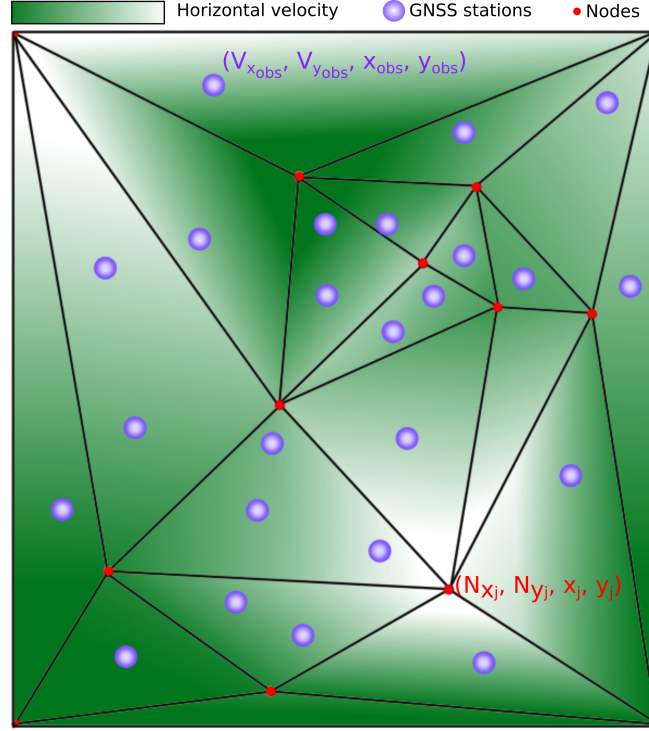


**Figure 2.** Example of surface meshing using Delaunay triangulation. Each node (in red) is assigned an horizontal velocity and the full velocity field (green gradient) can be obtained using a first order linear interpolation between the vertices on each triangle. Vertices can be added, suppressed or displaced during the algorithm, and their values can be modified. They are distinct from fixed GNSS stations (in purple) where data are available.

$$p(\mathbf{d}_{\text{obs}}|\mathbf{m}) \propto \exp\left(-\sum_{i \in [1,n]} \left(\frac{(V_{x_i} - S_{x_i}(\mathbf{m}))^2}{2\sigma_{x_i}^2} + \frac{(V_{y_i} - S_{y_i}(\mathbf{m}))^2}{2\sigma_{y_i}^2}\right)\right), \quad (3)$$

where  $S_{x_i}(\mathbf{m})$  and  $S_{y_i}(\mathbf{m})$  stand for the components of the surface velocity predicted by the model  $\mathbf{m}$  at the position of data points  $[x_i, y_i]$ . These values are compared with the observed velocities  $V_{x_i}$  and  $V_{y_i}$  at the same positions, the differences being weighted by the corresponding uncertainties on the velocities  $(\sigma_{x_i}, \sigma_{y_i})$ .

### 4.3 Sampling models from the posterior distribution

We use a Markov chain Monte Carlo (MCMC) scheme to generate a large ensemble of models which distribution asymptotically converges to the *a posteriori* PDF. Here we use the reversible-jump Markov chain Monte-Carlo algorithm (Green, 1995, 2003) which

**Algorithm 1** *rj-MCMC main loop*


---

Start with an initial model described by a set of vertices  $\mathbf{m}(N_{x_i}, N_{y_i}, x_i, y_i)$ .

**for**  $i = 1, N_{samples}$  **do**

**1** : Propose a new model  $\mathbf{m}$  by randomly perturbing the current model. Choose one of the following perturbation at random:

- Birth of a node on a random point of the surface.
- Death of a node.
- Change the horizontal velocity of a node.
- Displacement of a node.

**2** : Calculate the *a posteriori* probability of the perturbed model  $p(\mathbf{m}'|\mathbf{d}_{obs})$

**3** : Randomly accept the new model with probability  $\alpha(\mathbf{m}'|\mathbf{m}) = f\left(\frac{p(\mathbf{m}'|\mathbf{d}_{obs})}{p(\mathbf{m}|\mathbf{d}_{obs})}\right)$

where  $f(\cdot)$  is a function defined in Bodin & Sambridge (2009)

**4** : If accepted,  $\mathbf{m} \leftarrow \mathbf{m}'$ . Else,  $\mathbf{m} \leftarrow \mathbf{m}$ .

**5** : Compute the velocity field  $S(\mathbf{m})$  predicted for the model, and keep it in the ensemble solution. For each point of the map (i.e. on an underlying small grid as defined in section 4.4), calculate the velocity field at the point, its spatial derivatives, the strain rate tensor, and any quantity of interest (second invariant, divergence, vorticity, ...). Store these values for the final distribution.

**end for**

---

is a generalization of the Metropolis-Hasting algorithm (Metropolis et al., 1953; Hastings, 1970) to the case where the number of parameters is variable.

This algorithm randomly explores the model space by generating a chain of models where at each step, the current model is perturbed to produce a new proposed model. Then, the *a posteriori* probability of the current and proposed model are compared, and the new model is either accepted in the chain or rejected according to an acceptance rule depending on the ratio of posterior values. A pseudocode for the algorithm is given in table Algorithm 1 below. For a general description of MCMC sampling, see (Geyer, 1992; Brooks et al., 2011; Sambridge & Mosegaard, 2002). For specific applications to trans-dimensional geophysical problems where the number of parameter is variable, see (Bodin & Sambridge, 2009; Bodin, Sambridge, et al., 2012; Sambridge et al., 2013).

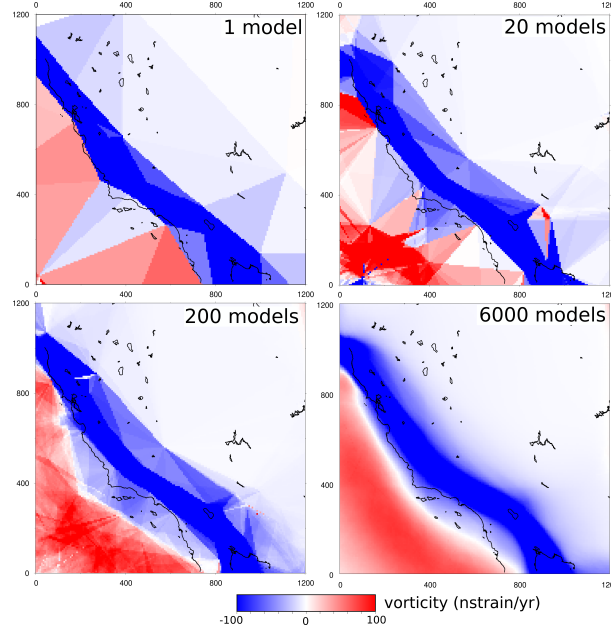


**Figure 3.** Convergence of the mean vorticity map. Convergence tests are performed on the synthetic velocity field built for our study area. Each panel shows the mean of the vorticity in the ensemble solution that is composed of either 1, 20, 200 or 6000 models. As the number of sampled models increases (i.e. the number of steps in the random walk), the relevant characteristics of the vorticity field begin to appear while the triangle-shaped areas due to the Delaunay triangulation tend to fade away.

As the number of iterations in the Markov chain increases, the values of sampled parameters (e.g. the number of nodes) progressively converge toward a statistically stationary distribution which approximates the posterior distribution.

#### 4.4 Extracting relevant information from the ensemble solution

It is important to note that the solution to our problem is not a single Delaunay velocity model that minimizes a misfit function. A model with zero misfit could be easily obtained by placing a Delaunay node at each GNSS station. However, such a model would be strongly unrealistic, as it would fit data errors, and depict a constant velocity gradient in each triangle, with sharp and discontinuous changes in strain rate at the triangle edges.

Instead, the solution of a Bayesian inverse problem is rather the entire *a posteriori* probability distribution (PDF), i.e. an ensemble of velocity models with varying num-

ber of Delaunay cells. To appraise this distribution, we define an underlying grid (which can be as fine as needed for visualization), and store at each pixel of the grid the full distribution of all parameters of interest, such as velocity components, spatial derivatives, divergence, vorticity,  $I_2$ , or any other combination of the strain tensor components. By combining the information from several tens of thousand of models, we therefore obtain at each pixel of the map the entire probability distribution on any desired parameter.

For visualization, we exhibit 2D maps of statistical indicators for the parameter of interest : the representation of the posterior PDF is, at each point of the map, the average, the median value or the mode of maximum probability from all sampled models on that point. As an example, the mean vorticity map obtained for the synthetic test case presented in section 5.1 is shown in Figure 3. In this way, a large number of models with different Delaunay parametrizations are stacked together. In a single model, the vorticity is constant over each triangle (top-left panel in Figure 3). But the continuous mean model contains features common to the entire family of models and considerably more information than any single Delaunay model.

Finally, it is important to insure that the algorithm has reasonably converged. A great number of models (typically between  $10^4$  and  $10^5$ ) are required to obtain an accurate depiction of the complete *a posteriori* probability distribution function. The influence of the number of models on the mean solution is shown in Figure 3, where the map of mean vorticity value is shown for different numbers of MCMC iterations.

## 5 Results

### 5.1 Synthetic tests on an ideal San Andreas Fault

In order to assess the efficiency of our algorithm, we build a synthetic velocity field that results from the relative plate motion and interseismic loading on a simplified San Andreas fault. We use the TDEFNODE code developed by McCaffrey (2005) and based on Okada (1985)'s equations, and assume full locking of the fault (from 0 to 30 km depth) within a fully elastic homogeneous half-space (see Figure 4 and 5). The fault is designed as vertical and is forced to be purely strike-slip. The Pacific plate motion relative to the fixed North American plate is described by an ad-hoc Euler pole (21.9°E, 14.2°N, 0.48°/Myr), that generates an overall 5 cm/yr relative right lateral motion.



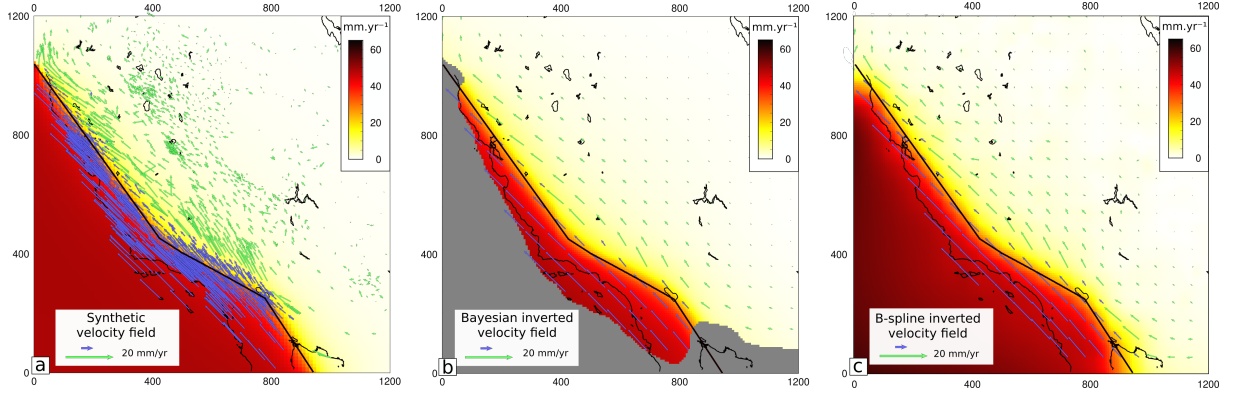


**Figure 4.** Synthetic tests for velocity field recovery on an idealized San Andreas fault. Black line : fault location. a) The amplitude of the synthetic horizontal velocity is color coded. Blue and green arrows stands for the synthetic velocity data sampled at the position of the GNSS stations from the real MIDAS velocity field. b) Average velocity field obtained with our Bayesian scheme. Areas where the PDF displays a standard deviation  $\geq 3\text{ mm/yr}$  are masked. c) Interpolated velocity field inverted with B-spline standard procedure.

We then extract the velocities at the locations of stations used in the MIDAS dataset (see section 3 and (Blewitt et al., 2016)), and add random Gaussian errors to each component with variance given by MIDAS uncertainties. We invert this synthetic data set to recover a continuous velocity field, its divergence, vorticity and the second invariant  $I_2$  of the strain rate tensor using two methods : our Bayesian algorithm presented above, and a standard bi-cubic spline-in-tension inversion method (see figures 4 and 5). In order to assess the quality of the inversion, we use the  $L_2$  distance between maps of second invariant for the recovered model and the true synthetic model:

$$Distance = \sqrt{\frac{1}{n} \sum_{i=1}^n (I_2^{true} - I_2^m)_i^2} \quad (4)$$

where  $I_2^{true}$  and  $I_2^m$  are the second invariants derived from the true synthetic model and the inverted velocity field, and  $n$  is the number of pixels in the maps. We chose to define the distance on  $I_2$  rather than on the velocity components since it appears that inversion artifacts appear on velocity spatial derivatives (Baxter et al., 2011). This distance indicates the ability of a method to recover the original signal over the entire region, though it does not reflect the level of data fit (measured only at stations).

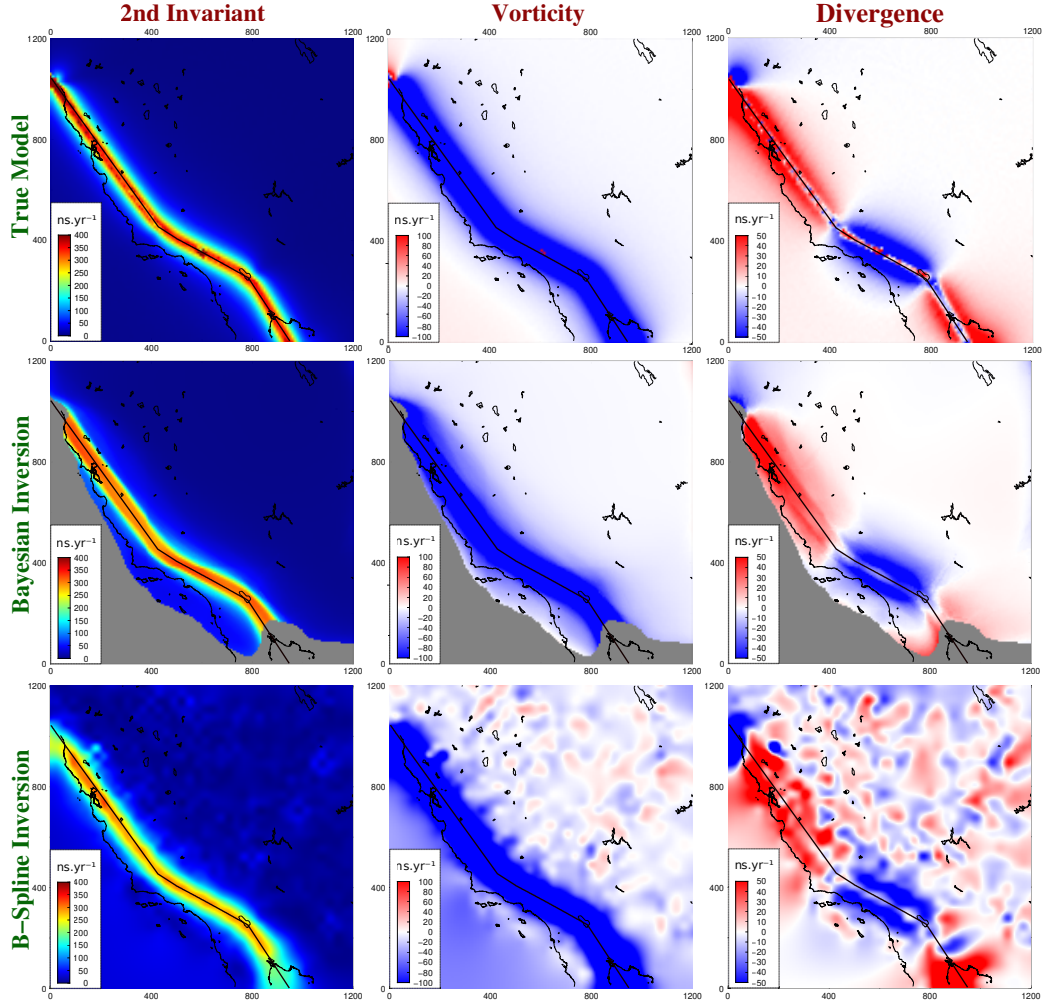


**Figure 5.** Strain rate tensor recovery from our synthetic test on an idealized San Andreas fault. Maps of the second invariant (left), vorticity (center) and divergence (right, compression is negative, dilation is positive) of the strain rate tensor are shown. The values expected from our synthetic model are shown on the upper panels (“True model”), together with results from our Bayesian inversion (average of the posterior distribution, middle), and from standard B-spline inversion (model obtained with optimal tension and grid parameters, lower panels). Black line : simplified San Andreas fault trace. Areas where the standard deviation of the horizontal velocity PDF is higher than 3 mm/yr are masked since our Bayesian inversion is insufficiently constrained there (see figure 4). Parameters of the B-spline inversion were chosen to minimize the distance to the true model on the second invariant (see equation 4).

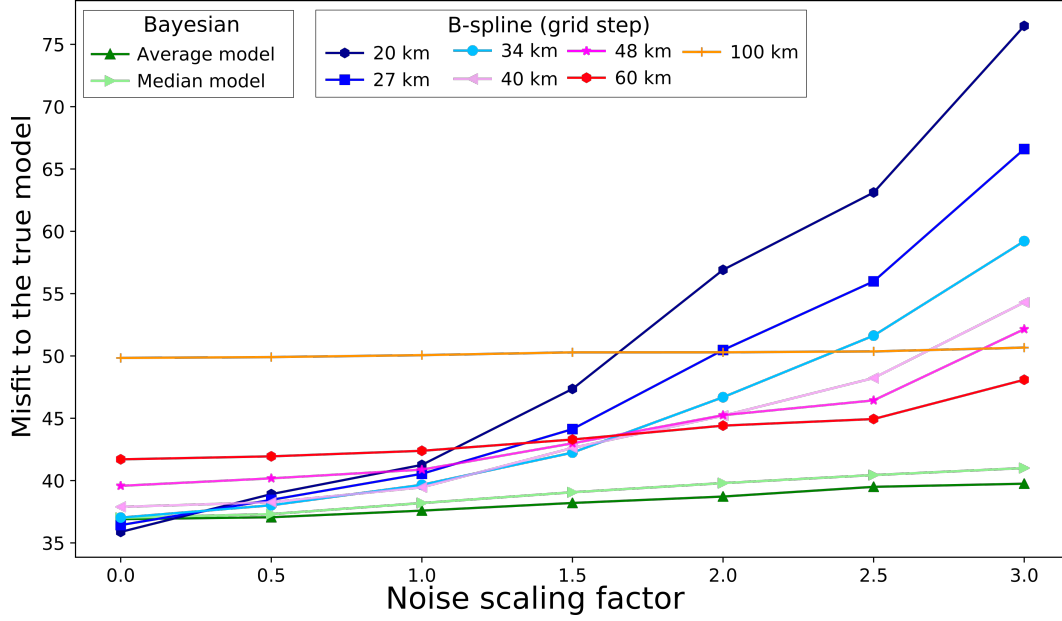


**Figure 6.** Distance to the true model calculated on the second invariant for the Bayesian inversion (based on the average model) and the B-spline method, for increasing level of data noise (see equation 4). Different B-spline inversions with increasing grid steps, corresponding to an increased level of smoothing are presented.

To perform the B-spline interpolation, we use a minimum curvature approach, where the interpolated surface minimized the level of data fit, while having continuous second derivatives and minimal total squared curvature (Smith & Wessel, 1990). We use the GMT *blockmean* and *surface* functions (Wessel et al., 2019), and calculate independently the velocity components  $V_{east}$  and  $V_{north}$  on each node of a predefined grid. In this procedure, the smoothness of the solution is determined by 2 parameters arbitrarily chosen by the user: the size of the grid and a tension parameter (see (Smith & Wessel, 1990) for more details on the method).

Those user-defined inputs are critical and should be carefully chosen. Therefore, on figures 4 and 5, we show the B-spline solution that minimizes the distance to the true model (equation 4), obtained by manually adjusting the tension and grid parameters. Of course, in a real data case, this manual adjustment could not be done.

For comparison, we plot on figures 4 and 5 the mean of the posterior PDF obtained with our Bayesian scheme for the velocity field, vorticity, divergence and second invariant. Overall, both inversion methods retrieve reasonably well the synthetic target with

a fit to the true  $I_2$  model of 37.6 and 39.5 nstrain/yr for the average of our Bayesian solution and B-spline best model, respectively. Though, major differences arise locally on spatial derivatives of the velocity field. Distributions obtained for  $I_2$ , vorticity and divergence inverted using B-spline inversion contain small wavelengths that are well known interpolation artifacts mainly due to network geometry and data outliers (Baxter et al., 2011). Moreover,  $I_2$  is systematically underestimated in the near field of the fault due to over-smoothing (by around 100 nstrain/yr), and the divergence map is particularly affected by small scale artifacts that may lead to incorrect interpretations. On the other hand, the average maps resulting from the Bayesian inversion are free from these small scale artifacts and recover well both the amplitude and spatial variations of deformation.

### 5.1.1 Noise sensitivity

One of the main limitation of conventional approaches used to produce strain rate maps is their high sensitivity to noise. As shown in Figure 5, the Bayesian inversion appears significantly more resilient to errors than the B-spline method. The patchy aspect of the divergence map obtained from the B-spline interpolation could be reduced by using a higher level of smoothing but meaningful signal in the near-field of the fault would then be lost.

We test the influence of the level of noise added to the synthetic data set on both inversion techniques. Random errors are kept Gaussian and uncorrelated between stations. We test different cases where we progressively increase the noise on the data by scaling the errors given by MIDAS uncertainties by a factor varying between 0 and 3. Because results from the B-spline interpolation highly depends on user-defined parameters, we systematically test different smoothing values (i.e. grid steps) for each noise level with a constant tension. We compare in figure 6 the results obtained for the B-spline and Bayesian method. For the Bayesian inversion, we represent both the average and the median of the  $I_2$  PDF.

As expected, the quality of both interpolations decreases with the level of noise. However, the Bayesian scheme performs better than the B-spline inversion, whatever the smoothing factor (i.e. grid step) considered. Figure 6 also illustrates well the sensitivity of the B-spline interpolation to the smoothing parameter (grid step) : low smoothing produces data over-fitting and unstable results, whereas high smoothing causes in-

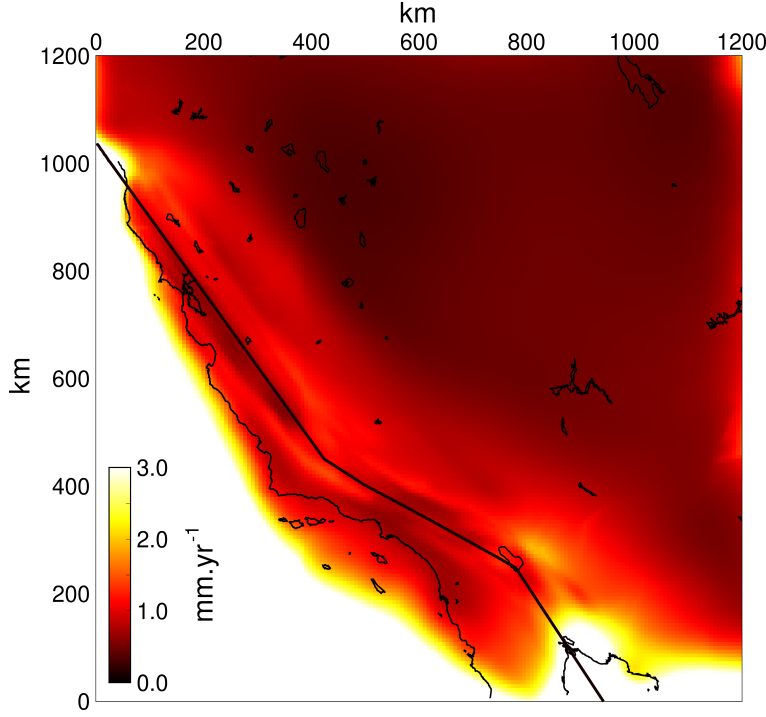


**Figure 7.** Standard deviation of the probability density function (PDF) obtained for the norm of the horizontal velocity using our Bayesian method on synthetic noisy data set (noise factor of 1). The color-scale is saturated for  $\sigma \geq 3 \text{ mm/yr}$ , this threshold help masking the poorly constrained areas in figures 5,4 and 9. Areas of high velocity gradients are characterized by intermediate standard deviations, while zones with no or few data exhibit higher standard deviations (e.g. edges of the studied area). This statistic measure can be used as a proxy for the robustness of the result (see figure 5).

formation loss. Our Bayesian inversion scheme enables us to avoid having to arbitrarily choose the level of complexity in the reconstructed model (Bodin & Sambridge, 2009).

### 5.1.2 Visualizing and interpreting the Posterior solution

Obtaining a comprehensive estimate of the posterior uncertainties affecting the interpolated velocity field and its spatial derivatives can be challenging. One option is to consider at each geographical point the standard deviation of the posterior PDF for each inverted parameter (velocity,  $I_2$ , vorticity, divergence). We plot in figure 7 this error map for the norm of the horizontal velocities. The standard deviation is the highest where data are scarce or missing : there, the solution is not constrained and the PDF is nearly

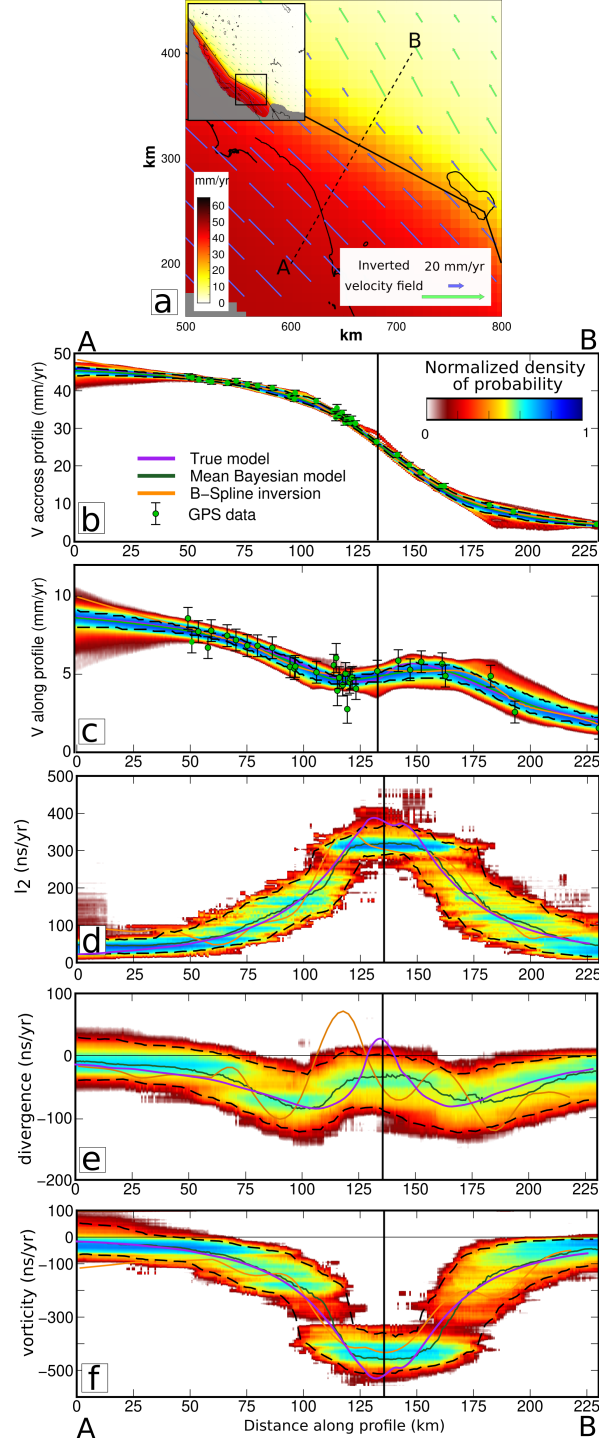


**Figure 8.** Slices of the entire PDF for different parameters along the cross-section displayed on top left of the picture. The location of the fault is materialized by a vertical black line on the profiles. The horizontal axis represents the distance along the section and the vertical axis corresponds to the range of the prior, i.e. the allowed range of values for the parameter. The color scale indicate the probability for the parameter on each point to take the corresponding value in the posterior. Profiles of the true model, the mean Bayesian model and the B-spline inversion are superposed on the PDF. The red dotted line delimits the interval of 90% confidence. a) PDF of the velocity, along and across profiles b) PDF of the  $2^{nd}$  invariant, the divergence and the vorticity of the strain rate tensor.

flat. We chose to mask these unconstrained zones based on a threshold value fixed at 3 mm/yr (see grey areas in figure 5 for instance). On the other hand, zones where the velocity field is well captured by the data set are characterized by low error values ( $\leq 0.5\text{mm/yr}$ ). Intermediate levels of errors are observed in areas where the velocity gradient is the highest, i.e. in the very near field from the San Andreas fault in our synthetic model.

A careful inspection of the posterior distribution can be conducted on areas of interest to better interpret the results. A convenient way to do so is to plot the full distribution on chosen cross-sections. In figure 8, we present the posterior distribution for both components of horizontal velocity (b-c), second invariant  $I_2$  (d), divergence (e) and vorticity (f) along a 230 km-long profile roughly perpendicular (azimuth N55) to the southernmost section of the San Andreas fault (see figure 8-a). The normalized probability distribution is color-coded for each pixel. The mean and 90% credible interval of the distribution are indicated as well as the result from the B-spline interpolation method and the true synthetic model. The posterior distributions for the velocity components are very narrow ( $< 1.5\text{mm/yr}$ ), and centered on the true model. The distribution is wider for the derivatives because small oscillations in the velocity field can lead to substantial variations on the components of the strain rate tensor. The true model is enclosed in the 90% confidence interval and is in general well estimated by the mean of the distribution, except in the very near field of the fault, where deformation is strongly localized.

Results from the B-spline interpolation often deviate significantly from the true model with misplaced or non-existent oscillations, that are directly due to noisy data and that correspond to the small-wavelength patches seen in figure 5. It is therefore difficult to conduct a proper interpretation of spatial derivatives of the velocity field obtained from direct interpolation schemes, especially since these artifacts resemble the signal that could be expected around active faults Baxter et al. (2011).

## 5.2 Bayesian inversion of the MIDAS dataset

We then invert the real observations from the MIDAS dataset (Blewitt et al., 2016) and associated uncertainties described in section 3. We present in figure 9 the map of posterior mean for  $I_2$  and the divergence (see supplementary material for map of the vorticity, standard deviation, and velocity residuals). Figure 10 shows the full distribution plotted along two distinct profiles crossing the San Andreas fault for the perpendicular-

to-profile velocity component and second invariant  $I_2$ . The recovered map of second invariant is rather smooth, except in the near field from the San Andreas fault zone. There, high values of  $I_2$  (higher than 1000 nstrain/yr) are observed on relatively narrow zones around the main fault (80 km wide for box 2 in figure 9 and corresponding cross-section in figure 10-b). An extreme situation is observed in the Monarch Peak segment (box 1 in figure 9) where  $I_2$  reaches values well above 1000 nstrain/yr on a 15 km narrow section around the main fault (see figure 10-a). In the Walker lane,  $I_2$  reaches intermediate values ( $\sim 100$  nstrain/yr) while it is lower than 10 nstrain/yr in the Basin and Range area with a slight increase over the Wasatch mountains. The profiles presented in figure 10 a and b cross the San Andreas fault Monarch Peak and Salton Sea lake segments, respectively. Both zones are relatively well constrained by the data set since the posterior distribution of the velocity components is narrow all along the profile line, except in the very near field of the fault in the Monarch Peak segment. Distributions are wider for  $I_2$ , in particular when crossing the active faults. The average, median and maximum probability are plotted, together with the 90% confidence interval. Differences are small between the average and median in the velocity profiles (less than 1mm/yr) and trends are very similar in  $I_2$  cross-section. Some significant variations arise when looking at the maximum probability mode that exhibits sharper transitions in particular in the Monarch Peak profile (figure 10-a).

The map showing the mean of the distribution for the divergence exhibits much more complex spatial variations (figure 9-b). Values range from -500 to 300 nstrain/yr, with extrema located in the vicinity of the San Andreas main fault zone (color scale is saturated in figure 9-b for clarity). Compression is dominant in the Garlock-San Andreas junction zone, while extension occurs at low rates in the Wasatch mountains in a nearly E-W direction. Slightly higher dilation rates are observed in the Walker Lane region (20-30 nstrain/yr) and in the Long Valley caldera (up to 200 nstrain/yr locally). Some localized extensional areas are also found in the vicinity of the main San Andreas fault zone in agreement with previously published dilatation maps (e.g. Kreemer et al., 2014).

In order to discuss the tectonic style in the area, we also compute the distribution for principal strain rate directions, and plot the mean directions in figure 9-b. Figure 11 shows a representation of the full distribution corresponding to box 3 in figure 9-b. Rose diagrams provide a convenient way to jointly plot the principal strain rate direction, its amplitude (length of the histogram bin), style (compression is blue, extension is red) and



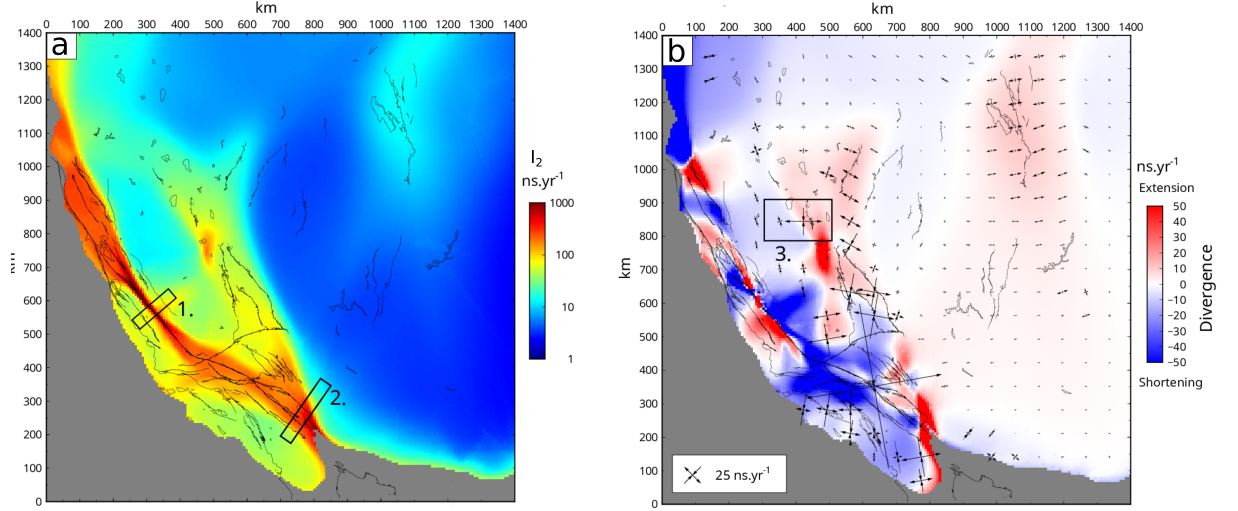


**Figure 9.** a- Average of the *a posteriori* probability distribution (PDF) of the second invariant of the strain rate tensor  $I_2$  in  $\text{ns.yr}^{-1}$ . The color scale is saturated for values above 1000  $\text{ns.yr}^{-1}$ . Black lines : active faults from Quaternary fault and fold database (2019). Box 1 and 2 stand for the chosen cross sections presented in figure 10 for the creeping segment north of Parkfield and Salton Sea Lake segments, respectively. b- Same but for the divergence. Positive divergence stands for extension, negative for compression. Black arrows : mean of the principal directions of the strain rate tensor for an arbitrarily chosen set of points, scaled by their amplitude. Box 3 is the area represented in figure 11.

the associated normalized probability (color coded, see figure 11). Therefore, one can assess how well constrained is the strain rate tensor and can assess whether the tectonic style is robustly defined : for instance, the dispersion is lower around the principal directions to the East (Sierra Nevada) than to the West (Walker Lane) in figure 11. There, a large dispersion is observed both in the direction of the principal strain and in their amplitude : while the maximum probability mode shows a dominant roughly N160 compression and a limited N70 extension, few models propose a dominant N110 extension and a limited N20 compression, i.e. a completely distinct tectonic regime. Such poorly constrained principal strain rate components should therefore be considered with extreme caution if used for tectonic interpretation.

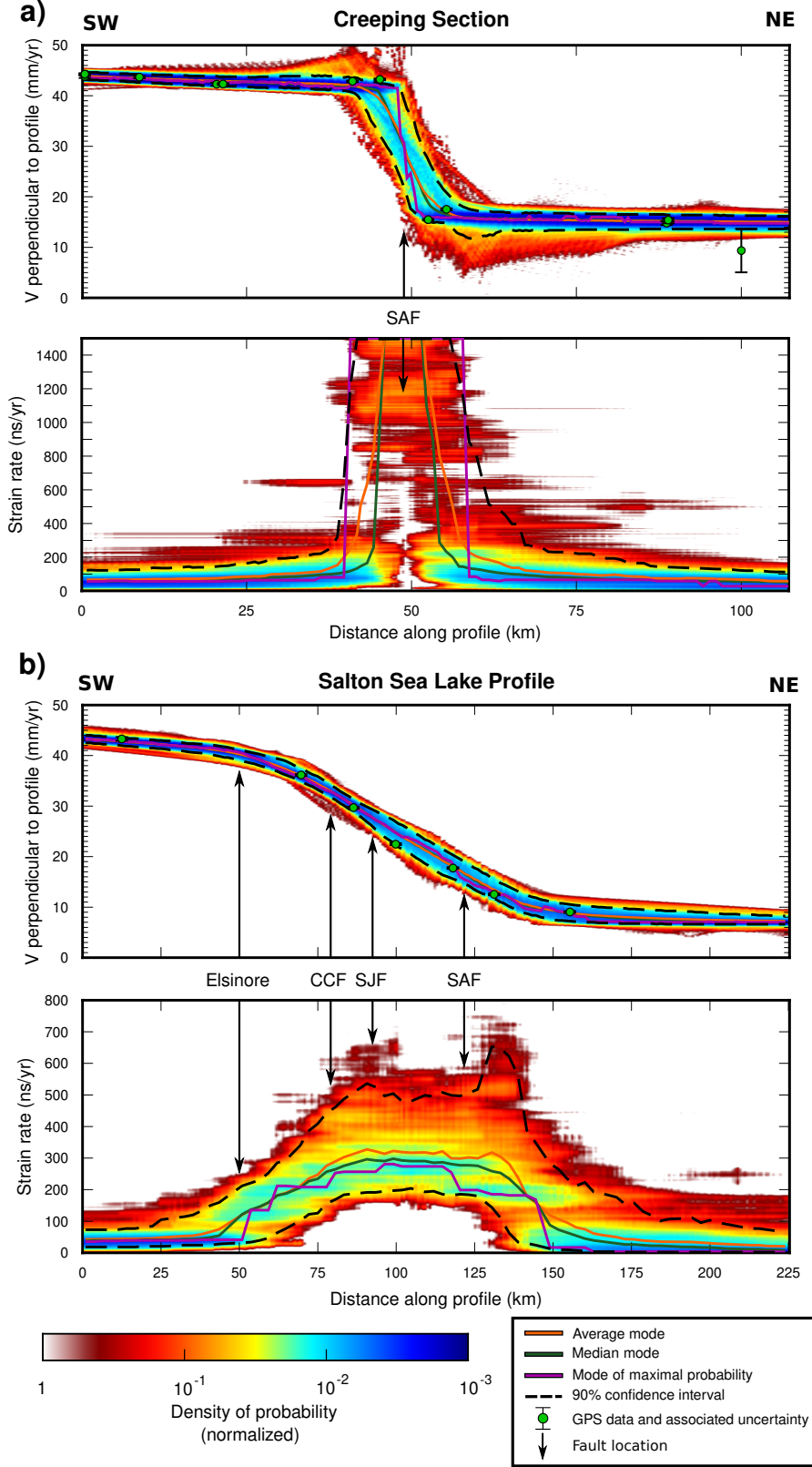


**Figure 10.** Variations of the perpendicular velocity component (upper panel) and  $I_2$  (bottom panel) along two profile lines shown in figure 9. The full posterior probability (normalized) plotted together with its average (orange line), median (green line), maximum (purple) and 90% of probability envelop (dashed black line). Black arrows stand for the main mapped faults (Quaternary fault and fold database, 2019; Fialko, 2006) : SAF San Andreas fault, SJF : San Jacinto fault, CCF : Coyote Creek fault, and Elsinore fault.

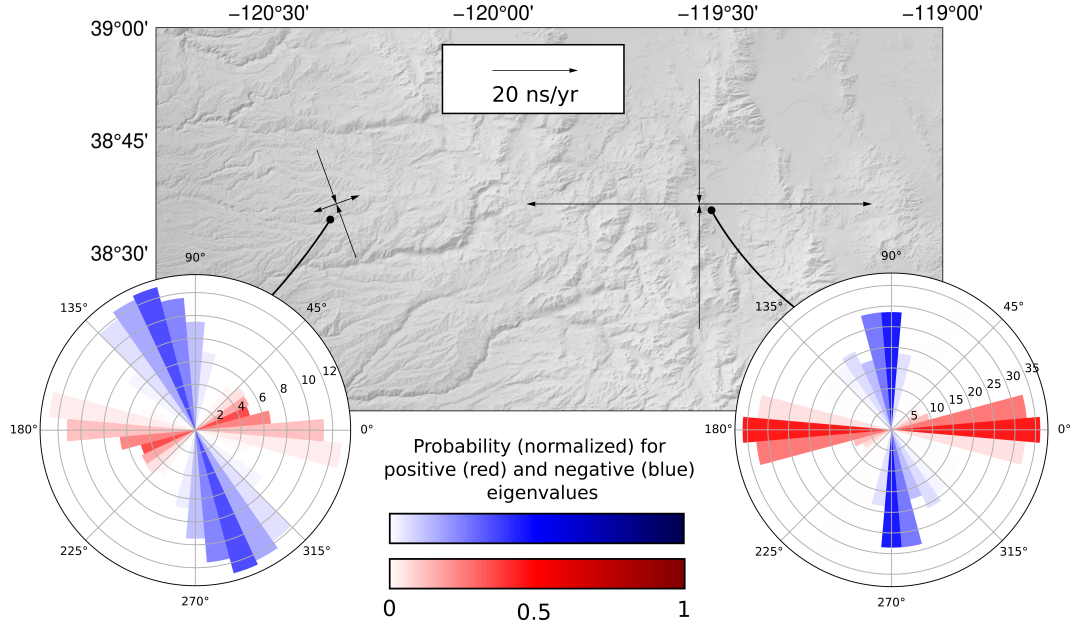


**Figure 11.** Zoom on the Sierra Nevada to Walker Lane transition, i.e. zone 3 in figure 9-b. Black arrows stand for the average of the PDF for the principal components of the strain rate tensor. A more complete description of the PDF is proposed as windroses for both points : the amplitude (in nstrain/yr) and normalized probability (color coded) is represented for each 10° bin. Blue stand for compression, red for extension.

## 6 Discussion

### 6.1 Advantages and limits of the Bayesian surface reconstruction

As shown with synthetic tests, our method provides better strain rate estimates compared to conventional interpolations schemes, where the level of smoothing is manually adjusted by the user. In a transdimensional formulation, the number of parameters defining the surface is not fixed in advance, and the complexity of the solution (smoothness) naturally adapts to the level of information present in the data. A probabilistic solution also provides a full description of uncertainties for any parameter of interests (here, vorticity, divergence, etc). In particular, our approach can provide uncertainty estimates on the largest eigenvalue of the strain rate tensor, which is used in the Kostrov formulation for geodetic moment rate calculation (Kostrov, 1974; D’Agostino, 2014). Several PSHA techniques are now starting to integrate geodetic estimates of surface strain Beauval et al. (2018) : the full posterior distribution for principal directions, velocity derivatives and strain rate invariants could directly be included in logic trees.

However, our method is based on a Monte Carlo sampling scheme where a large number of Delaunay models are tested against the data, and is therefore computationally intensive. Our final ensemble solution represented in figure 9 is obtained after 84 hours of calculation on 92 parallel processors, which is much larger than standard interpolation approaches.

We shall also acknowledge that a Bayesian formulation is entirely based on the mathematical model used to describe the statistics of data errors. In this study, we assume errors are Gaussian, and uncorrelated between different stations and between each horizontal component. A more accurate model could be used by accounting for the spatial correlation of errors in regional velocity fields (Wdowinski et al., 1997; Williams et al., 2004; Dong et al., 2006; Santamaría-Gómez et al., 2011; Benoist et al., 2020). This can be done by using a full covariance matrix of data errors in the likelihood function Bodin, Sambridge, et al. (2012). A Bayesian scheme naturally propagates errors in the data towards errors in the posterior solution, and the form of the probabilistic solution also depends on the estimated amplitude of data uncertainties. If data errors are misestimated, posterior uncertainties will be also misestimated. In this work, we followed a conservative approach and increased the uncertainties provided by MIDAS by 10%. In the case

where the level of data errors is poorly known, this level could be treated as an unknown in the inversion (Bodin, Salmon, et al., 2012).

We shall also note that the method presented in this study has been implemented in cartesian coordinates, i.e. assuming the effect of Earth’s sphericity is negligible. This hypothesis remains valid when focusing on relatively small regions but the code should be adapted to spherical coordinates if to be applied to larger continental-scale regions (e.g. Haines & Holt, 1993; Kreemer et al., 2014; H. Wang et al., 2019).

## 6.2 From a probabilistic solution to tectonic interpretations

The method is applied to one of the most extensively studied area in terms of active tectonics : the San Andreas strike-slip fault system and the neighboring Basin and Range extensional area (see section 3 and references therein). The maps of second invariant and divergence presented in figure 9 agree with previous studies (e.g. Holt et al., 2000; McCaffrey, 2005; Kreemer & Hammond, 2007; Kreemer et al., 2012) and which have been compared by Sandwell et al. (2010). We confirm that (i) transtension is dominant in the Walker Lane (Wesnousky et al., 2012), (ii) the innermost Basin and Range (Central Great Basin) experiences very low strain rates and could therefore be considered as rigid (Bennett et al., 2003), and (iii) 10 nstrain/yr roughly E-W extension occurs in the Wasatch mountains (Niemi et al., 2004). Our results tend to show that the Central Valley and Sierra Nevada are not behaving as a purely rigid block (Bennett et al., 2003; Kreemer et al., 2014) but accommodate some amount of NNW-SSE directed compression ( $I_2 \geq 10$  nstrain/yr).

In addition, our mean map of second invariant depicts very clear along strike variations in the width of the highly straining area near the main fault of the San Andreas system that are consistent with along-strike segmentation. In particular, our results confirm that creep occurs in the Monarch Peak segment (Ben-Zion et al., 1993; Rolandone et al., 2008; Jolivet et al., 2015) that is surrounded by rather locked fault systems north and south of it. To investigate further the ability of our method to capture along-strike segmentation without *a priori* information on the fault position, we plot in figure 10 the full PDF for  $I_2$  and for the perpendicular-to-profile velocity along two cross-sections located in the Monarch Peak and Salton Sea segments (box 1 and box 2 in figure 9, respectively). The surface velocity gradient from one side of the fault to the other (between

40 mm/yr and 45 mm/yr depending on the considered segment) is accommodated on a 80 km wide zone around the Salton Sea segment while it is concentrated on a narrow 15 km wide zone in the Monarch Peak creeping segment. There, the expected velocity change should be even more abrupt (as seen from InSAR images for instance, (Jolivet et al., 2015)) but the GNSS network is not sufficiently dense to capture changes over lower than 15 km baselines. However, interestingly, the mode of maximum probability exhibits such an abrupt change while average and median of the PDF are smoother (figure 10-a). The second invariant  $I_2$  as seen in cross section in this creeping segment increases abruptly well above 1000 nstrain/yr starting around 10 km from the fault on each side.

In the Salton Sea Lake area, several faults are parallel to the main San Andreas fault and potentially active (see figure 10-b) : identifying the amount of relative motion that is taken by each of these structures is still debated (Fialko, 2006; Lundgren et al., 2009; Lindsey & Fialko, 2013) and is needed to properly conduct seismic hazard assessment. For instance, Lindsey & Fialko (2013) explore several physical models with distinct fault geometries or spatial heterogeneities in the crustal elastic properties to estimate the fault slip on each of these faults based on the inversion of GPS and InSAR surface velocities. The ambiguity between those models comes from the very similar resulting surface velocity field. However, these models predict larger differences in surface strain rate that could be better observed looking at the fit to the second invariant  $I_2$  for instance. This requires uncertainties on  $I_2$  to be correctly estimated, as in figure 10-b.

The Bayesian method developed in this study allows us to identify creeping segments from locking segments and potentially active faults during the interseismic period without a priori constraints on the structure of deformation. It is to note that it jointly retrieves the velocity field and its derivatives in areas of large strain rates such as the San Andreas fault system, but also in areas of lower deformation rates such as the Wasatch mountains experiencing  $\sim 20$  nstrain/yr extension. It appears robust enough to discuss with confidence second order features of the strain rate tensor that could be meaningful in well resolved areas. For instance, it has been proposed for years that the surface strain pattern above an active locked fault could show some level of asymmetry depending on the rheology and lithology contrast between both blocks (Le Pichon et al., 2005; Fialko, 2006; Chéry, 2008; Jolivet et al., 2008). The posterior distribution for velocity or second invariant could show whether this asymmetry is required by the data.

Furthermore, having access to the uncertainties associated with the principal strain directions will help comparing deformation over broader time-scale and discuss more finely how strain is partitioned on active structures. However, this method is primarily dependent on the density and quality of observations, which remains the limiting factor in such discussions.

### 6.3 Future developments

The development of modern geodetic techniques in the last decades (GNSS continuously recording networks, satellite images, tiltmeters) has led to the generalisation of strain rate maps based on velocities averaged on several years that are discussed in very broad contexts : long-term tectonics (e.g. Kreemer et al., 2003; Flesch & Kreemer, 2010), seismic cycle (e.g. D’Agostino, 2014; H. Wang et al., 2019; Klein et al., 2019), or hydrology (e.g. Silverii et al., 2020). Recently, strain rates have been calculated on much shorter time-spans in order to capture the surface deformation associated with phenomena such as ground water variations (Klein et al., 2019; Silverii et al., 2020), magmatic intrusions (Silverii et al., 2019) or slow-slip events (e.g. Delbridge et al., 2020). Our interpolation method, with its ability to properly account for data errors, could prove useful in these cases where observations are associated with larger than usual uncertainties.

The algorithm presented in this study has been designed for and applied to GNSS horizontal velocity fields. It could also be applied to a variety of interpolation problems in the geosciences, providing correct estimates of uncertainties. For instance, one could easily apply our proposed approach to the interpolation of horizontal coseismic displacements and associated strain tensor. Recently, Barnhart et al. (2020b) use high-resolution optical images correlation technique to recover the horizontal coseismic displacement associated with the Ridgecrest earthquake sequence that stroke the East California Shear Zone and Garlock fault in 2019 (Mw 6.4 and Mw 7.1 for the main shocks). Their interpretation of the derived dilatation maps in terms of inelastic deformation in the very near field from the fault is highlighted by Feng & Almeida (2020) since it would have important consequences on our understanding of faults and earthquakes. However, as previously shown, dilatation maps are prone to strong interpolation artifacts and should be carefully interpreted, or built with our artifact-free method.

The next step is therefore to adapt our technique to more continuous pictures of the surface deformation as produced by optical correlation (e.g. Vallage et al., 2015; De-  
 lorme et al., 2020; Barnhart et al., 2020b) or by InSAR (LOS velocities). One difficulty  
 to do so is to properly account for the correlation between pixels, fully described by a  
 covariance matrix (Hussain et al., 2016; H. Wang et al., 2019). Second, these images of  
 surface deformation often offer a description of the vertical velocity field (or displace-  
 ment) or a combination of horizontal and vertical velocities in the LOS direction. Our  
 method should therefore be adapted to jointly interpolate the three components of the  
 velocity field (including the vertical velocities coming from high quality GNSS measure-  
 ments). The implementation is relatively straightforward and will be added in the fu-  
 ture, though it will add computational cost. Including vertical velocities will give us ac-  
 cess to the horizontal derivatives of  $V_z$  that could help identifying active faults, subsi-  
 dence and uplift patterns. However, even with this more complete view of the 3D strain  
 rate tensor, this latter will remain incomplete as derivative with respect to the vertical  
 direction will be missing. Note that some attempts to take into account the horizontal  
 gradients of vertical velocity into a pseudo 3D strain rate tensor have been conducted  
 by Mazzotti et al. (2005); Shen & Liu (2020) or Piña-Valdés et al. (2020) and could be  
 implemented in the future.

## 7 Conclusion

We develop a transdimensional Bayesian method, adapted from seismic imaging  
 (Bodin, Salmon, et al., 2012; Bodin, Sambridge, et al., 2012) to estimate surface strain  
 rates from discrete GNSS horizontal velocity fields. Synthetic tests conducted on an ide-  
 alized velocity field produced by the interseismic locking of the San Andreas fault zone  
 show that this approach is more robust than an standard B-spline interpolation tech-  
 nique. In particular, it is able to correctly recover the strain rate tensor on a wide range  
 of rates, without need of manually tuned user-defined parameters. The solution is a full  
 probability distribution on model parameters defining the velocity field and its spacial  
 derivatives. We propose several ways to visualize the solution through maps of the mean,  
 median, standard deviation, or maximum probability. We also show cross-sections pre-  
 senting the full posterior distribution. The probability distribution of principal directions  
 of strain rates can be plotted on wind rose diagrams, allowing for a better comparison  
 with longer-term tectonic studies.



We apply our method to the MIDAS velocity dataset on the San Andreas and Basin and Range area and find that, while in general agreement with previously published strain rate maps, our results are smoother and artifact free. They allow for safer tectonic interpretation, and help discriminating between creeping and locked fault segments. Our Bayesian inversion method designed to solve this very common interpolation and derivation problem will be applied in future work to continuous images of deformation like InSAR or optical correlations, that could be combined together. We hope that the proposed approach will allow to take full profit of geodetic measurements and to include them better in probabilistic seismic hazard assessment techniques.

## Acknowledgments

This work has been supported by the Programme National de Télédétection Spatiale (PNTS, <http://www.insu.cnrs.fr/pnts>), grant n°PNTS-2019-7. It has been conducted in the frame of the European Union’s Horizon2020 research and innovation programme under grant agreement no.716542. Most figures have been done using the open source Generic Mapping Tool software <https://www.generic-mapping-tools.org/>.

## References

- Altamimi, Z., Métivier, L., Rebischung, P., Rouby, H., & Collilieux, X. (2017). Itrf2014 plate motion model. *Geophysical Journal International*, 209(3), 1906–1912.
- Altamimi, Z., Rebischung, P., Métivier, L., & Collilieux, X. (2016). Itrf2014: A new release of the international terrestrial reference frame modeling nonlinear station motions. *Journal of Geophysical Research: Solid Earth*, 121(8), 6109–6131.
- Amos, C. B., Audet, P., Hammond, W. C., Bürgmann, R., Johanson, I. A., & Blewitt, G. (2014). Uplift and seismicity driven by groundwater depletion in central california. *Nature*, 509(7501), 483–486.
- Angelica, C., Bonforte, A., Distefano, G., Serpelloni, E., & Gresta, S. (2013). Seismic potential in Italy from integration and comparison of seismic and geodetic strain rates. *Tectonophysics*, 608, 996–1006.
- Aster, R. C., Borchers, B., & Thurber, C. H. (2018). *Parameter estimation and inverse problems*. Elsevier.
- Avouac, J.-P. (2015). From geodetic imaging of seismic and aseismic fault slip to dy-

- 766        namic modeling of the seismic cycle. *Annual Review of Earth and Planetary Sci-*  
 767        *ences*, *43*, 233–271.
- 768        Barnhart, W. D., Gold, R. D., & Hollingsworth, J. (2020a). Localized fault-zone  
 769        dilatancy and surface inelasticity of the 2019 ridgecrest earthquakes. *Nature Geo-*  
 770        *science*, *13*(10), 699–704.
- 771        Barnhart, W. D., Gold, R. D., & Hollingsworth, J. (2020b). Localized fault-zone  
 772        dilatancy and surface inelasticity of the 2019 ridgecrest earthquakes. *Nature Geo-*  
 773        *science*, *13*(10), 699–704.
- 774        Baxter, S. C., Kedar, S., Parker, J. W., Webb, F. H., Owen, S. E., Sibthorpe, A.,  
 775        & Dong, D. (2011). Limitations of strain estimation techniques from discrete  
 776        deformation observations. *Geophysical Research Letters*, *38*(1).
- 777        Beauval, C., Marinière, J., Yepes, H., Audin, L., Nocquet, J.-M., Alvarado, A., ...  
 778        Jomard, H. (2018). A new seismic hazard model for ecuador. *Bulletin of the*  
 779        *Seismological Society of America*, *108*(3A), 1443–1464.
- 780        Beavan, J., & Haines, J. (2001). Contemporary horizontal velocity and strain rate  
 781        fields of the pacific-australian plate boundary zone through new zealand. *Journal*  
 782        *of Geophysical Research: Solid Earth*, *106*(B1), 741–770.
- 783        Bennett, R. A., & Hreinsdóttir, S. (2007). Constraints on vertical crustal motion for  
 784        long baselines in the central mediterranean region using continuous gps. *Earth and*  
 785        *Planetary Science Letters*, *257*(3-4), 419–434.
- 786        Bennett, R. A., Wernicke, B., Niemi, N., Friedrich, A., & Davis, J. (2003). Contem-  
 787        porary strain rates in the northern basin and range province from gps data. *Tec-*  
 788        *tonics*, *22*(2).
- 789        Benoist, C., Collilieux, X., Rebischung, P., Altamimi, Z., Jamet, O., Métivier, L., ...  
 790        Bel, L. (2020). Accounting for spatiotemporal correlations of gnss coordinate time  
 791        series to estimate station velocities. *Journal of Geodynamics*, *135*, 101693.
- 792        Ben-Zion, Y., Rice, J. R., & Dmowska, R. (1993). Interaction of the san andreas  
 793        fault creeping segment with adjacent great rupture zones and earthquake re-  
 794        currence at parkfield. *Journal of Geophysical Research: Solid Earth*, *98*(B2),  
 795        2135–2144.
- 796        Blewitt, G., Hammond, W. C., & Kreemer, C. (2018). Harnessing the gps data ex-  
 797        plosion for interdisciplinary science. *Eos*, *99*, 1–2.
- 798        Blewitt, G., Kreemer, C., Hammond, W. C., & Gazeaux, J. (2016). Midas robust

- 799 trend estimator for accurate gps station velocities without step detection. *Journal*  
800 *of Geophysical Research: Solid Earth*, 121(3), 2054–2068.
- 801 Bodin, T., Salmon, M., Kennett, B., & Sambridge, M. (2012). Probabilistic surface  
802 reconstruction from multiple data sets: an example for the australian moho. *Jour-*  
803 *nal of Geophysical Research: Solid Earth*, 117(B10).
- 804 Bodin, T., & Sambridge, M. (2009). Seismic tomography with the reversible jump  
805 algorithm. *Geophysical Journal International*, 178(3), 1411–1436.
- 806 Bodin, T., Sambridge, M., Rawlinson, N., & Arroucau, P. (2012). Transdimensional  
807 tomography with unknown data noise. *Geophysical Journal International*, 189(3),  
808 1536–1556.
- 809 Brooks, S., Gelman, A., Jones, G., & Meng, X.-L. (2011). *Handbook of markov chain*  
810 *monte carlo*. CRC press.
- 811 Bürgmann, R., & Thatcher, W. (2013). Space geodesy: A revolution in crustal  
812 deformation measurements of tectonic processes. *Geol. Soc. Am. Spec. Pap.*, 500,  
813 397–430.
- 814 Cai, J., Wang, J., Wu, J., Hu, C., Grafarend, E., & Chen, J. (2008). Horizontal de-  
815 formation rate analysis based on multiepoch gps measurements in shanghai. *Jour-*  
816 *nal of Surveying Engineering*, 134(4), 132–137.
- 817 Chaussard, E., Milillo, P., Bürgmann, R., Perissin, D., Fielding, E. J., & Baker,  
818 B. (2017). Remote sensing of ground deformation for monitoring groundwater  
819 management practices: Application to the santa clara valley during the 2012–  
820 2015 california drought. *Journal of Geophysical Research: Solid Earth*, 122(10),  
821 8566–8582.
- 822 Chéry, J. (2008). Geodetic strain across the san andreas fault reflects elastic plate  
823 thickness variations (rather than fault slip rate). *Earth and Planetary Science Let-*  
824 *ters*, 269(3-4), 352–365.
- 825 Chlieh, M., Avouac, J.-P., Sieh, K., Natawidjaja, D. H., & Galetzka, J. (2008).  
826 Heterogeneous coupling of the sumatran megathrust constrained by geodetic and  
827 paleogeodetic measurements. *Journal of Geophysical Research: Solid Earth*,  
828 113(B5).
- 829 Choblet, G., Husson, L., & Bodin, T. (2014). Probabilistic surface reconstruction  
830 of coastal sea level rise during the twentieth century. *Journal of Geophysical Re-*  
831 *search: Solid Earth*, 119(12), 9206–9236.

- 832 Chousianitis, K., Ganas, A., & Evangelidis, C. P. (2015). Strain and rotation rate  
833 patterns of mainland greece from continuous gps data and comparison between  
834 seismic and geodetic moment release. *Journal of Geophysical Research: Solid*  
835 *Earth*, *120*(5), 3909–3931.
- 836 Copley, A. (2008). Kinematics and dynamics of the southeastern margin of the ti-  
837 betan plateau. *Geophysical Journal International*, *174*(3), 1081–1100.
- 838 D’Agostino, N. (2014). Complete seismic release of tectonic strain and earthquake  
839 recurrence in the apennines (italy). *Geophysical Research Letters*, *41*(4), 1155–  
840 1162.
- 841 D’Agostino, N., England, P., Hunstad, I., & Selvaggi, G. (2014). Gravitational po-  
842 tential energy and active deformation in the apennines. *Earth and planetary sci-*  
843 *ence letters*, *397*, 121–132.
- 844 Delbridge, B. G., Carmichael, J. D., Nadeau, R. M., Shelly, D. R., & Bürgmann,  
845 R. (2020). Geodetic measurements of slow-slip events southeast of parkfield, ca.  
846 *Journal of Geophysical Research: Solid Earth*, *125*(5), e2019JB019059.
- 847 Delorme, A., Grandin, R., Klinger, Y., Pierrot-Deseilligny, M., Feillet, N., Jacques,  
848 E., ... Morishita, Y. (2020). Complex deformation at shallow depth during the 30  
849 october 2016 mw6.5 norcia earthquake: interference between tectonic and gravity  
850 processes? *Tectonics*, *39*(2), e2019TC005596.
- 851 Dong, D., Fang, P., Bock, Y., Webb, F., Prawirodirdjo, L., Kedar, S., & Jamason,  
852 P. (2006). Spatiotemporal filtering using principal component analysis and  
853 karhunen-loeve expansion approaches for regional gps network analysis. *Journal of*  
854 *geophysical research: solid earth*, *111*(B3).
- 855 Elliott, J., Walters, R., & Wright, T. (2016). The role of space-based observation  
856 in understanding and responding to active tectonics and earthquakes. *Nature com-*  
857 *munications*, *7*(1), 1–16.
- 858 England, P., Houseman, G., & Nocquet, J.-M. (2016). Constraints from gps mea-  
859 surements on the dynamics of deformation in anatolia and the aegean. *Journal of*  
860 *Geophysical Research: Solid Earth*, *121*(12), 8888–8916.
- 861 England, P., & Molnar, P. (1997). Active deformation of asia: From kinematics to  
862 dynamics. *Science*, *278*(5338), 647–650.
- 863 Farolfi, G., & Del Ventisette, C. (2017). Strain rates in the alpine mediterranean re-  
864 gion: Insights from advanced techniques of data processing. *GPS solutions*, *21*(3),

- 1027–1036.
- Feng, W., & Almeida, R. V. (2020). Inelastic earthquake damage. *Nature Geoscience*, 13(10), 661–662.
- Fialko, Y. (2006). Interseismic strain accumulation and the earthquake potential on the southern san andreas fault system. *Nature*, 441(7096), 968–971.
- Flesch, L. M., & Kreemer, C. (2010). Gravitational potential energy and regional stress and strain rate fields for continental plateaus: Examples from the central andes and colorado plateau. *Tectonophysics*, 482(1-4), 182–192.
- Frank, F. (1966). Deduction of earth strains from survey data. *Bulletin of the Seismological Society of America*, 56(1), 35–42.
- Freymueller, J. T., Murray, M. H., Segall, P., & Castillo, D. (1999). Kinematics of the pacific-north america plate boundary zone, northern california. *Journal of Geophysical Research: Solid Earth*, 104(B4), 7419–7441.
- Gan, W., Zhang, P., Shen, Z.-K., Niu, Z., Wang, M., Wan, Y., ... Cheng, J. (2007). Present-day crustal motion within the tibetan plateau inferred from gps measurements. *Journal of Geophysical Research: Solid Earth*, 112(B8).
- Gerstenberger, M. C., Marzocchi, W., Allen, T., Pagani, M., Adams, J., Danciu, L., ... others (2020). Probabilistic seismic hazard analysis at regional and national scales: State of the art and future challenges. *Reviews of Geophysics*, 58(2), e2019RG000653.
- Geyer, C. J. (1992). Practical markov chain monte carlo. *Statistical science*, 473–483.
- Green, P. J. (1995). Reversible jump markov chain monte carlo computation and bayesian model determination. *Biometrika*, 82(4), 711–732.
- Green, P. J. (2003). Trans-dimensional markov chain monte carlo. *Oxford Statistical Science Series*, 179–198.
- Hackl, M., Malservisi, R., & Wdowinski, S. (2009). Strain rate patterns from dense gps networks. *Natural Hazards Earth Systems Sciences*, 9, 1177.
- Haines, A., & Holt, W. (1993). A procedure for obtaining the complete horizontal motions within zones of distributed deformation from the inversion of strain rate data. *Journal of Geophysical Research: Solid Earth*, 98(B7), 12057–12082.
- Hammond, B., Blewitt, G., Kreemer, C., Bormann, J., & Jha, S. (2010). The magnet gps network gps velocities. *Sierra*, 37, 38.

- 898 Hammond, W., Kreemer, C., Zaliapin, I., & Blewitt, G. (2019). Drought-triggered  
899 magmatic inflation, crustal strain, and seismicity near the long valley caldera,  
900 central walker lane. *Journal of Geophysical Research: Solid Earth*, 124(6), 6072–  
901 6091.
- 902 Hammond, W. C., Blewitt, G., & Kreemer, C. (2016). Gps imaging of vertical land  
903 motion in california and nevada: Implications for sierra nevada uplift. *Journal of*  
904 *Geophysical Research: Solid Earth*, 121(10), 7681–7703.
- 905 Hastings, W. K. (1970). Monte carlo sampling methods using markov chains and  
906 their applications.
- 907 Hawkins, R., Bodin, T., Sambridge, M., Choblet, G., & Husson, L. (2019). Trans-  
908 dimensional surface reconstruction with different classes of parameterization. *Geo-*  
909 *chemistry, Geophysics, Geosystems*, 20(1), 505–529.
- 910 Hawkins, R., Husson, L., Choblet, G., Bodin, T., & Pfeffer, J. (2019). Virtual tide  
911 gauges for predicting relative sea level rise. *Journal of Geophysical Research: Solid*  
912 *Earth*, 124(12), 13367–13391.
- 913 Herring, T. A., Melbourne, T. I., Murray, M. H., Floyd, M. A., Szeliga, W. M.,  
914 King, R. W., . . . Wang, L. (2016). Plate boundary observatory and related net-  
915 works: Gps data analysis methods and geodetic products. *Reviews of Geophysics*,  
916 54(4), 759–808.
- 917 Holt, W., Chamot-Rooke, N., Le Pichon, X., Haines, A., Shen-Tu, B., & Ren, J.  
918 (2000). Velocity field in asia inferred from quaternary fault slip rates and global  
919 positioning system observations. *Journal of Geophysical Research: Solid Earth*,  
920 105(B8), 19185–19209.
- 921 Hudnut, K. W., Bock, Y., Galetzka, J. E., Webb, F. H., & Young, W. H. (2001).  
922 The southern california integrated gps network (scign). In *The 10th fig interna-*  
923 *tional symposium on deformation measurements* (pp. 19–22).
- 924 Hussain, E., Hooper, A., Wright, T. J., Walters, R. J., & Bekaert, D. P. (2016).  
925 Interseismic strain accumulation across the central north anatolian fault from it-  
926 eratively unwrapped insar measurements. *Journal of Geophysical Research: Solid*  
927 *Earth*, 121(12), 9000–9019.
- 928 Husson, L., Bodin, T., Spada, G., Choblet, G., & Kreemer, C. (2018). Bayesian  
929 surface reconstruction of geodetic uplift rates: Mapping the global fingerprint of  
930 glacial isostatic adjustment. *Journal of Geodynamics*, 122, 25–40.

- 931 Isacks, B., Oliver, J., & Sykes, L. R. (1968). Seismology and the new global tecton-  
932 ics. *Journal of Geophysical Research*, 73(18), 5855–5899.
- 933 Jolivet, R., Cattin, R., Chamot-Rooke, N., Lasserre, C., & Peltzer, G. (2008). Thin-  
934 plate modeling of interseismic deformation and asymmetry across the altyn tagh  
935 fault zone. *Geophysical Research Letters*, 35(2).
- 936 Jolivet, R., Simons, M., Agram, P., Duputel, Z., & Shen, Z.-K. (2015). Aseismic  
937 slip and seismogenic coupling along the central san andreas fault. *Geophysical Re-*  
938 *search Letters*, 42(2), 297–306.
- 939 Kaneko, Y., Avouac, J.-P., & Lapusta, N. (2010). Towards inferring earthquake pat-  
940 terns from geodetic observations of interseismic coupling. *Nature Geoscience*, 3(5),  
941 363–369.
- 942 Klein, E., Bock, Y., Xu, X., Sandwell, D. T., Golriz, D., Fang, P., & Su, L. (2019).  
943 Transient deformation in california from two decades of gps displacements: Impli-  
944 cations for a three-dimensional kinematic reference frame. *Journal of Geophysical*  
945 *Research: Solid Earth*, 124(11), 12189–12223.
- 946 Kostrov, V. (1974). Seismic moment and energy of earthquakes, and seismic flow of  
947 rock. *Izv. Acad. Sci. USSR Phys. Solid Earth, Engl. Transl.*, 1, 23–44.
- 948 Kreemer, C., Blewitt, G., & Klein, E. C. (2014). A geodetic plate motion and global  
949 strain rate model. *Geochemistry, Geophysics, Geosystems*, 15(10), 3849–3889.
- 950 Kreemer, C., & Hammond, W. C. (2007). Geodetic constraints on areal changes  
951 in the pacific–north america plate boundary zone: What controls basin and range  
952 extension? *Geology*, 35(10), 943–946.
- 953 Kreemer, C., Hammond, W. C., & Blewitt, G. (2018). A robust estimation of the  
954 3-d intraplate deformation of the north american plate from gps. *Journal of Geo-*  
955 *physical Research: Solid Earth*, 123(5), 4388–4412.
- 956 Kreemer, C., Hammond, W. C., Blewitt, G., Holland, A. A., & Bennett, R. A.  
957 (2012). A geodetic strain rate model for the pacific-north american plate bound-  
958 ary, western united states. *EGUGA*, 6785.
- 959 Kreemer, C., Holt, W. E., & Haines, A. J. (2003). An integrated global model of  
960 present-day plate motions and plate boundary deformation. *Geophysical Journal*  
961 *International*, 154(1), 8–34.
- 962 Le Pichon, X. (1968). Sea-floor spreading and continental drift. *Journal of Geophys-*  
963 *ical Research*, 73(12), 3661–3697.

- 964 Le Pichon, X., Kreemer, C., & Chamot-Rooke, N. (2005). Asymmetry in elastic  
965 properties and the evolution of large continental strike-slip faults. *Journal of Geo-*  
966 *physical Research: Solid Earth*, 110(B3).
- 967 Lindsey, E., & Fialko, Y. (2013). Geodetic slip rates in the southern san andreas  
968 fault system: Effects of elastic heterogeneity and fault geometry. *Journal of Geo-*  
969 *physical Research: Solid Earth*, 118(2), 689–697.
- 970 Lundgren, P., Hetland, E. A., Liu, Z., & Fielding, E. J. (2009). Southern san  
971 andreas-san jacinto fault system slip rates estimated from earthquake cycle mod-  
972 els constrained by gps and interferometric synthetic aperture radar observations.  
973 *Journal of Geophysical Research: Solid Earth*, 114(B2).
- 974 Machette, M. N., Personius, S. F., Nelson, A. R., Schwartz, D. P., & Lund, W. R.  
975 (1991). The wasatch fault zone, utah—segmentation and history of holocene  
976 earthquakes. *Journal of Structural Geology*, 13(2), 137–149.
- 977 Marshall, G. A., Langbein, J., Stein, R. S., Lisowski, M., & Svarc, J. (1997). Infla-  
978 tion of long valley caldera, california, basin and range strain, and possible mono  
979 craters dike opening from 1990–94 gps surveys. *Geophysical Research Letters*,  
980 24(9), 1003–1006.
- 981 Masson, C., Mazzotti, S., Vernant, P., & Doerflinger, E. (2019). Extracting small  
982 deformation beyond individual station precision from dense global navigation  
983 satellite system (gnss) networks in france and western europe. *Solid Earth*, 10(6),  
984 1905–1920.
- 985 Mathey, M., Walpersdorf, A., Sue, C., Baize, S., & Deprez, A. (2020). Seismogenic  
986 potential of the high durance fault constrained by 20 yr of gnss measurements in  
987 the western european alps. *Geophysical Journal International*, 222(3), 2136–2146.
- 988 Mazzotti, S., Déprez, A., Henrion, E., Masson, C., Masson, F., Menut, J.-L., ... oth-  
989 ers (2020). *Comparative analysis of synthetic gnss time series-bias and precision*  
990 *of velocity estimations* (Unpublished doctoral dissertation). RESIF.
- 991 Mazzotti, S., James, T. S., Henton, J., & Adams, J. (2005). Gps crustal strain, post-  
992 glacial rebound, and seismic hazard in eastern north america: The saint lawrence  
993 valley example. *Journal of Geophysical Research: Solid Earth*, 110(B11).
- 994 Mazzotti, S., Leonard, L., Cassidy, J., Rogers, G., & Halchuk, S. (2011). Seismic  
995 hazard in western canada from gps strain rates versus earthquake catalog. *Journal*  
996 *of Geophysical Research: Solid Earth*, 116(B12).



- 997 McCaffrey, R. (2005). Block kinematics of the pacific–north america plate boundary  
998 in the southwestern united states from inversion of gps, seismological, and geologic  
999 data. *Journal of Geophysical Research: Solid Earth*, 110(B7).
- 1000 McCaffrey, R., King, R. W., Payne, S. J., & Lancaster, M. (2013). Active tecton-  
1001 ics of northwestern us inferred from gps-derived surface velocities. *Journal of Geo-  
1002 physical Research: Solid Earth*, 118(2), 709–723.
- 1003 Metois, M., D’Agostino, N., Avallone, A., Chamot-Rooke, N., Rabaute, A., Duni, L.,  
1004 ... Georgiev, I. (2015). Insights on continental collisional processes from gps data:  
1005 Dynamics of the peri-adriatic belts. *Journal of Geophysical Research: Solid Earth*,  
1006 120(12), 8701–8719.
- 1007 Métois, M., Vigny, C., & Socquet, A. (2016). Interseismic coupling, megathrust  
1008 earthquakes and seismic swarms along the chilean subduction zone (38–18 s). *Pure  
1009 and Applied Geophysics*, 173(5), 1431–1449.
- 1010 Metropolis, N., Rosenbluth, A. W., Rosenbluth, M. N., Teller, A. H., & Teller, E.  
1011 (1953). Equation of state calculations by fast computing machines. *The journal of  
1012 chemical physics*, 21(6), 1087–1092.
- 1013 Milliner, C., & Donnellan, A. (2020). Using daily observations from planet labs  
1014 satellite imagery to separate the surface deformation between the 4 july m w 6.4  
1015 foreshock and 5 july m w 7.1 mainshock during the 2019 ridgecrest earthquake  
1016 sequence. *Seismological Research Letters*, 91(4), 1986–1997.
- 1017 Morgan, W. J. (1968). Rises, trenches, great faults, and crustal blocks. *Journal of  
1018 Geophysical Research*, 73(6), 1959–1982.
- 1019 Murray, J., & Langbein, J. (2006). Slip on the san andreas fault at parkfield, califor-  
1020 nia, over two earthquake cycles, and the implications for seismic hazard. *Bulletin  
1021 of the Seismological Society of America*, 96(4B), S283–S303.
- 1022 Niemi, N. A., Wernicke, B. P., Friedrich, A. M., Simons, M., Bennett, R. A., &  
1023 Davis, J. L. (2004). Bergen continuous gps data across the eastern basin and  
1024 range province, and implications for fault system dynamics. *Geophysical Journal  
1025 International*, 159(3), 842–862.
- 1026 Okada, Y. (1985). Surface deformation due to shear and tensile faults in a half-  
1027 space. *Bulletin of the seismological society of America*, 75(4), 1135–1154.
- 1028 Palano, M., Imprescia, P., Agnon, A., & Gresta, S. (2018). An improved evalua-  
1029 tion of the seismic/geodetic deformation-rate ratio for the zagros fold-and-thrust

- collisional belt. *Geophysical Journal International*, 213(1), 194–209.
- Pancha, A., Anderson, J. G., & Kreemer, C. (2006). Comparison of seismic and geodetic scalar moment rates across the basin and range province. *Bulletin of the Seismological Society of America*, 96(1), 11–32.
- Parsons, T. (2006). Tectonic stressing in california modeled from gps observations. *Journal of Geophysical Research: Solid Earth*, 111(B3).
- Peltzer, G., Crampé, F., Hensley, S., & Rosen, P. (2001a). Transient strain accumulation and fault interaction in the eastern california shear zone. *Geology*, 29(11), 975–978.
- Peltzer, G., Crampé, F., Hensley, S., & Rosen, P. (2001b). Transient strain accumulation and fault interaction in the eastern california shear zone. *Geology*, 29(11), 975–978.
- Pérouse, E., Chamot-Rooke, N., Rabaute, A., Briole, P., Jouanne, F., Georgiev, I., & Dimitrov, D. (2012). Bridging onshore and offshore present-day kinematics of central and eastern mediterranean: implications for crustal dynamics and mantle flow. *Geochemistry, Geophysics, Geosystems*, 13(9).
- Pérouse, E., & Wernicke, B. P. (2017). Spatiotemporal evolution of fault slip rates in deforming continents: The case of the great basin region, northern basin and range province. *Geosphere*, 13(1), 112–135.
- Piña-Valdés, J., Socquet, A., Beauval, C., Bard, P.-Y., Doin, M.-P., & Shen, Z. (2020). Toward the development of earthquake recurrence models from 3d gnss velocity field in europe. In *Egu general assembly conference abstracts* (p. 19808).
- Rolandone, F., Bürgmann, R., Agnew, D., Johanson, I., Templeton, D., d’Alessio, M., . . . Tikoff, B. (2008). Aseismic slip and fault-normal strain along the central creeping section of the san andreas fault. *Geophysical Research Letters*, 35(14).
- Sagiya, T., Miyazaki, S., & Tada, T. (2000). Continuous gps array and present-day crustal deformation of japan. *Pure and applied Geophysics*, 157(11-12), 2303–2322.
- Sambridge, M., Bodin, T., Gallagher, K., & Tkalčić, H. (2013). Transdimensional inference in the geosciences. *Philosophical Transactions of the Royal Society A: Mathematical, Physical and Engineering Sciences*, 371(1984), 20110547.
- Sambridge, M., & Mosegaard, K. (2002). Monte carlo methods in geophysical inverse problems. *Reviews of Geophysics*, 40(3), 3–1.

- 1063 Sandwell, D., Becker, T., Bird, P., Freed, A., Hackl, M., Holt, W., ... others (2010).  
 1064 Comparison of 16 strain-rate maps of southern california. *SCEC Presentation*,  
 1065 1(5).
- 1066 Santamaría-Gómez, A., Bouin, M.-N., Collilieux, X., & Wöppelmann, G. (2011).  
 1067 Correlated errors in gps position time series: Implications for velocity estimates.  
 1068 *Journal of Geophysical Research: Solid Earth*, 116(B1).
- 1069 Savage, J. (1983). A dislocation model of strain accumulation and release at a sub-  
 1070 duction zone. *Journal of Geophysical Research*, 88(3), 4984–4996.
- 1071 Savage, J., & Burford, R. (1970). Accumulation of tectonic strain in california. *Bul-*  
 1072 *letin of the Seismological Society of America*, 60(6), 1877–1896.
- 1073 Shen, Z.-K., Jackson, D. D., Feng, Y., Cline, M., Kim, M., Fang, P., & Bock, Y.  
 1074 (1994). Postseismic deformation following the landers earthquake, california, 28  
 1075 june 1992. *Bulletin of the Seismological Society of America*, 84(3), 780–791.
- 1076 Shen, Z.-K., Jackson, D. D., & Ge, B. X. (1996). Crustal deformation across and  
 1077 beyond the los angeles basin from geodetic measurements. *Journal of Geophysical*  
 1078 *Research: Solid Earth*, 101(B12), 27957–27980.
- 1079 Shen, Z.-K., Jackson, D. D., & Kagan, Y. Y. (2007). Implications of geodetic strain  
 1080 rate for future earthquakes, with a five-year forecast of m5 earthquakes in south-  
 1081 ern california. *Seismological Research Letters*, 78(1), 116–120.
- 1082 Shen, Z.-K., & Liu, Z. (2020). Integration of gps and insar data for resolving 3-  
 1083 dimensional crustal deformation. *Earth and Space Science*, 7(4), e2019EA001036.
- 1084 Shen, Z.-K., Wang, M., Zeng, Y., & Wang, F. (2015). Optimal interpolation of spa-  
 1085 tially discretized geodetic data. *Bulletin of the Seismological Society of America*,  
 1086 105(4), 2117–2127.
- 1087 Silverii, F., D’Agostino, N., Borsa, A. A., Calcaterra, S., Gambino, P., Giuliani,  
 1088 R., & Mattone, M. (2019). Transient crustal deformation from karst aquifers  
 1089 hydrology in the apennines (italy). *Earth and Planetary Science Letters*, 506,  
 1090 23–37.
- 1091 Silverii, F., Montgomery-Brown, E., Borsa, A., & Barbour, A. (2020). Hydrologically  
 1092 induced deformation in long valley caldera and adjacent sierra nevada. *Journal of*  
 1093 *Geophysical Research: Solid Earth*, 125(5).
- 1094 Simons, M., Minson, S., Sladen, A., Ortega, F., Jiang, J., Owen, S., ... oth-  
 1095 ers (2011). The 2011 magnitude 9.0 Tohoku-Oki earthquake: Mosaicking

- the megathrust from seconds to centuries. *Science*, 332(6036), 1421. doi:  
10.1126/science.1206731
- Smith, W., & Wessel, P. (1990). Gridding with continuous curvature splines in tension. *Geophysics*, 55(3), 293–305.
- Snay, R. A., Cline, M. W., & Timmerman, E. L. (1983). Regional deformation of the earth model for the san diego region, california. *Journal of Geophysical Research: Solid Earth*, 88(B6), 5009–5024.
- Spakman, W., & Nyst, M. (2002). Inversion of relative motion data for estimates of the velocity gradient field and fault slip. *Earth and Planetary Science Letters*, 203(1), 577–591.
- Tarantola, A. (2005). *Inverse problem theory and methods for model parameter estimation*. SIAM.
- Thatcher, W. (2009). How the continents deform: The evidence from tectonic geodesy. *Annual Review of Earth and Planetary Sciences*, 37.
- U.s. geological survey and new mexico bureau of mines and mineral resources, *quaternary fault and fold database for the united states*, accessed sept 1, 2019. (2019). Retrieved from <https://www.usgs.gov/natural-hazards/earthquake-hazards/faults>
- Vallage, A., Klinger, Y., Grandin, R., Bhat, H., & Pierrot-Deseilligny, M. (2015). Inelastic surface deformation during the 2013 mw 7.7 balochistan, pakistan, earthquake. *Geology*, 43(12), 1079–1082.
- Vergnolle, M., Calais, E., & Dong, L. (2007). Dynamics of continental deformation in asia. *Journal of Geophysical Research: Solid Earth*, 112(B11).
- Wang, H., Wright, T. J., Liu-Zeng, J., & Peng, L. (2019). Strain rate distribution in south-central tibet from two decades of insar and gps. *Geophysical Research Letters*, 46(10), 5170–5179.
- Wang, K., & Bürgmann, R. (2020). Co-and early postseismic deformation due to the 2019 ridgecrest earthquake sequence constrained by sentinel-1 and cosmo-skymed sar data. *Seismological Research Letters*, 91(4), 1998–2009.
- Ward, S. N. (1998). On the consistency of earthquake moment rates, geological fault data, and space geodetic strain: the united states. *Geophysical Journal International*, 134(1), 172–186.

- 1128 Wdowinski, S., Bock, Y., Zhang, J., Fang, P., & Genrich, J. (1997). Southern  
 1129 california permanent gps geodetic array: Spatial filtering of daily positions for  
 1130 estimating coseismic and postseismic displacements induced by the 1992 landers  
 1131 earthquake. *Journal of Geophysical Research: Solid Earth*, 102(B8), 18057–  
 1132 18070.
- 1133 Weiss, J. R., Walters, R. J., Morishita, Y., Wright, T. J., Lazecky, M., Wang, H.,  
 1134 ... others (2020). High-resolution surface velocities and strain for anatolia  
 1135 from sentinel-1 insar and gnss data. *Geophysical Research Letters*, 47(17),  
 1136 e2020GL087376.
- 1137 Wesnousky, S. G., Bormann, J. M., Kreemer, C., Hammond, W. C., & Brune, J. N.  
 1138 (2012). Neotectonics, geodesy, and seismic hazard in the northern walker lane  
 1139 of western north america: Thirty kilometers of crustal shear and no strike-slip?  
 1140 *Earth and Planetary Science Letters*, 329, 133–140.
- 1141 Wessel, P., & Becker, J. (2008). Interpolation using a generalized green’s function for  
 1142 a spherical surface spline in tension. *Geophysical Journal International*, 174(1),  
 1143 21–28.
- 1144 Wessel, P., & Bercovici, D. (1998). Interpolation with splines in tension: a green’s  
 1145 function approach. *Mathematical Geology*, 30(1), 77–93.
- 1146 Wessel, P., Luis, J., Uieda, L., Scharroo, R., Wobbe, F., Smith, W., & Tian, D.  
 1147 (2019). The generic mapping tools version 6. *Geochemistry, Geophysics, Geosys-*  
 1148 *tems*, 20(11), 5556–5564.
- 1149 Williams, S. D., Bock, Y., Fang, P., Jamason, P., Nikolaidis, R. M., Prawirodirdjo,  
 1150 L., ... Johnson, D. J. (2004). Error analysis of continuous gps position time  
 1151 series. *Journal of Geophysical Research: Solid Earth*, 109(B3).